

Modelling articular cartilage: the relative motion of two adjacent poroviscoelastic layers

JONATHAN P. WHITELEY

Department of Computer Science, University of Oxford, Wolfson Building, Parks Road, Oxford OX1 3QD, UK

CAMERON P. BROWN

MMPE, MERF, Faculty of Engineering, Queensland University of Technology, Brisbane, QLD 4000, Australia

AND

EAMONN A. GAFFNEY

Mathematical Institute, University of Oxford, Andrew Wiles Building, Radcliffe Observatory Quarter, Woodstock Road, Oxford OX2 6GG, UK

*Corresponding author: Jonathan.Whiteley@cs.ox.ac.uk

[Received on 15 December 2021; revised on 26 April 2022]

In skeletal joints two layers of adjacent cartilage are often in relative motion. The individual cartilage layers are often modelled as a poroviscoelastic material. To model the relative motion, noting the separation of scales between the pore level and the macroscale, a homogenization based on multiple scale asymptotic analysis has been used in this study to derive a macroscale model for the relative translation of two poroviscoelastic layers separated by a very thin layer of fluid. In particular the fluid layer thickness is essentially zero at the macroscale so that the two poroviscoelastic layers are effectively in contact and their interaction is captured in the derived model via a set of interfacial conditions, including a generalization of the Beavers–Joseph condition at the interface between a viscous fluid and a porous medium. In the simplifying context of a uniform geometry, constant fixed charge density, a Newtonian interstitial fluid and a viscoelastic scaffold, modelled via finite deformation theory, we present preliminary simulations that may be used to highlight predictions for how oscillatory relative movement of cartilage under load influences the peak force the cartilage experiences and the extent of the associated deformations. In addition to highlighting such cartilage mechanics, the systematic derivation of the macroscale models will enable the study of how nanoscale cartilage physics, such as the swelling pressure induced by fixed charges, manifests in cartilage mechanics at much higher lengthscales.

Keywords: cartilage; poroviscoelasticity; homogenization.

1. Introduction

Opposing bone surfaces in a joint are covered by layers of articular cartilage of thickness around 1–3 mm, which bear loads of up to 18 MPa or 180 kg/cm² with remarkably low coefficients of friction (0.002–0.01) over the loading cycles of a lifetime (Hodge *et al.*, 1986). Fundamental in supporting such mechanical extremes is the structure of articular cartilage, which consists of a heterogeneous, anisotropic matrix of collagen, meshed with a network of proteoglycans, mainly aggrecan, possessing a bottlebrush side chain structure of charged glycoaminoglycans (Mow *et al.*, 1992; Klika *et al.*, 2016).

The glycoaminoglycan charge induces a large swelling pressure placing the collagen scaffold under tensile stress, thus allowing the cartilage to resist load with interstitial fluid squeezed out (Harrigan & Mann, 1987). This system can be represented at a continuum level by biphasic models, with solid and interstitial phases, as well as triphasic models with an additional charge phase, as pioneered in the modelling framework developed by Mow and colleagues (Mow *et al.*, 1980a,b, 1986, 1989; Ateshian *et al.*, 1997). In turn this framework has been extensively reviewed (Ateshian, 2009; Klika *et al.*, 2016) and has been subject to diverse and extensive investigations by numerous groups, as we briefly and incompletely illustrate by mentioning studies of further validation and experimental comparison (Ateshian *et al.*, 1997; DiSilvestro & Francis Suh, 2001; Huang *et al.*, 2003; Lu *et al.*, 2020), thermodynamic consistency (Huyghe *et al.*, 2009), distinct positive and negative charge phases (Huyghe & Janssen, 1997), anisotropy and heterogeneity (Wilson *et al.*, 2005; Nagel & Kelly, 2010; Klika *et al.*, 2019), as well as the development of finite element modelling simulation platforms (Wu *et al.*, 1998; Ateshian *et al.*, 2013).

In addition to withstanding load, articular cartilage is vital for the lubrication of shearing bone movement within a joint, ensuring it occurs with a low friction coefficient. Diverse mechanisms for this mechanical performance have been contemplated, many of which are based on a lubricating synovial fluid layer such as hydrodynamic and elastohydrodynamic lubrication. Another class of mechanism is boundary lubrication, in which charged long chain molecules, either in the synovial fluid or at the cartilage surface, induce a surface lubrication of opposing articular cartilage (Mow *et al.*, 1993; Forster & Fisher, 1999). However, indications are that, according to context, there is either boundary lubrication or a mixed mode lubrication with spatially heterogeneous lubrication: boundary lubrication in some regions of opposing cartilage and a lubricating synovial fluid layer in others (Gleghorn & Bonassar, 2008). Both categories of lubrication are supplemented with ‘biphasic’ lubrication (Mow *et al.*, 1993) where the fluid phase supports the majority of the load, thus reducing the load and concomitant friction of the solid phase (Forster & Fisher, 1999).

Despite such extensive study there has been relatively limited modelling and simulation of the mechanics of opposing articular cartilage in shear. Analytical studies have focused on loading rather than shear (Ateshian *et al.*, 1994), which nonetheless have supported the concept of biphasic lubrication, while further studies have contributed to explaining numerous aspects of friction coefficients given an assumption that friction is proportional to the normal load supported by the solid phase (Ateshian, 1997, 2009; Ateshian *et al.*, 1994, 1998); in contrast, recent detailed modelling has focused on the computational fluid dynamics between the cartilage layers (Wu & Ferguson, 2017; Liao *et al.*, 2019, 2020).

Our focus within such wide ranging studies concerns a recent investigation that revisited elements of the fundamental triphasic modelling, using homogenization theory to explicitly determine how a continuum macroscale model relates to the microscale and nanoscale physics of cartilage (Whiteley & Gaffney, 2020). In particular this study derived a nonlinear finite deformation poroviscoelastic continuum model, which systematically incorporated: the impact of the swelling pressure due to glycoaminoglycan fixed charge; solid collagen, as represented by a Voigt viscoelastic solid; and a viscous Newtonian interstitial fluid. However, the subsequent examination of the mechanics of this homogenized poroviscoelastic model, including its associated constitutive relations, only considered 1D compression tests. Here our main objective is to generalize this homogenized poroviscoelastic model to conditions of opposing cartilage shear, which is relevant not only for joint motion but also experimental studies of joint and artificial joint motion, as in Ateshian *et al.* (1998) for example. In particular to examine cartilage in relative shearing motion separated by fluid, as occurs in mixed mode lubrication (albeit not necessarily everywhere), one first needs boundary conditions between the synovial fluid and

the cartilage. Thus our main objective requires us to determine these boundary conditions, which is more generally relevant for modelling the shearing of homogenized models for poroviscoelastic bodies.

In a related problem, the Beavers–Joseph condition (Beavers & Joseph, 1967) supplies an empirically derived interface condition for the tangential slip velocity at the interface between a viscous fluid and porous body when the flow is driven by the free fluid flowing over the porous bed, while Hou *et al.* (1989) derived an analogous condition for a shearing interface between a viscous fluid and a biphasic material. In particular, the Beavers–Joseph condition may be written as

$$\mu \frac{\partial u_t}{\partial x_n} = \frac{\alpha}{\sqrt{K}} (u_t - u_t^D),$$

where μ is the dynamic viscosity of the fluid, \mathbf{u} is the velocity of the free fluid, \mathbf{u}^D is the Darcy fluid flux in the porous body, \mathbf{x} represents the spatial coordinates, K is an averaged isotropic permeability of the porous body in a thin layer close to the interface (which may be different to the permeability in the interior of the porous body (Lacis & Bagheri, 2017)), α is a constant that depends only on properties of the porous material, the subscripts t, n represent the tangential and normal directions, respectively, and the normal points out of the porous body into the free fluid. Saffman (1971) pointed out that the magnitude of the fluid flux in the porous body is much smaller than the magnitude of the free fluid velocity, allowing the u_t^D term in the Beavers–Joseph condition to be neglected. Theoretical work (Mikelić & Jäger, 2000; Auriault, 2010; Lacis & Bagheri, 2017) is in agreement with the Saffman modification of the Beavers–Joseph condition. There are, however, additional terms in the interface condition proposed by Lacis & Bagheri (2017) because this work considers a free fluid Reynolds number that is $\mathcal{O}(1)$; other work assumes low Reynolds number flow, i.e. Stokes flow, in the free fluid. Related work (Marciniak-Czochra & Mikelić, 2012; Carraro *et al.*, 2013) derives other conditions that are required at the interface between the fluid and the porous body, such as continuity or otherwise of the fluid pressure across the interface.

We thus generalize the results described in the studies above to the interface between two poroviscoelastic bodies that are separated by a thin layer of synovial fluid, as is seen in skeletal joints and illustrated in Fig. 1, to determine the analogue of the Beavers–Joseph boundary condition together with the other, simpler, boundary conditions that are required. This allows the modelling of relative shear between two homogenized poroviscoelastic bodies bathed in interstitial fluid. We use the conditions derived to conduct an initial examination of the mechanics associated with such motion, in particular that motivated by shearing cartilage motion within a joint.

As we use a variety of coordinate systems and model several physical processes at different scales we begin by summarizing the notation and conventions that are used in this paper in Section 2. The governing equations in the cartilage region, describing large deformation poroviscoelasticity, are written down in Section 3. A mathematical model of the synovial fluid region and the transition layers in the cartilage regions close to the synovial fluid region is written down in Section 4. By using a multiple scales analysis of this model in Section 5, we demonstrate that the synovial fluid may be modelled as an interface with zero thickness between the two layers of cartilage, and derive appropriate interface conditions. Numerical simulations using these interface conditions are presented in Section 6. We conclude by summarizing our findings in Section 7.

2. Notation used

A summary of the key notation used is given in Table 1; other notation will be defined when it first appears. We consider two separate lengthscales in this study. The macro lengthscale is the lengthscale

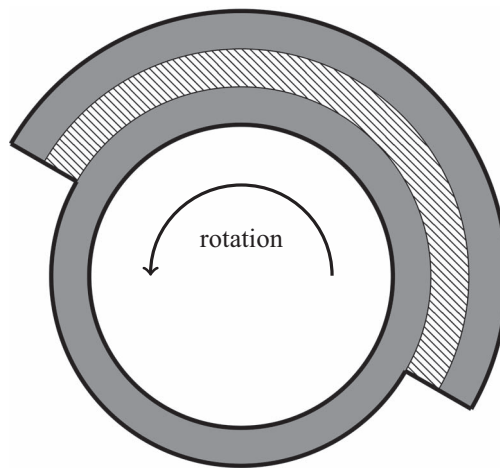


FIG. 1. Schematic diagram of a hip joint. The grey regions represent cartilage, and the hatched region represents synovial fluid. The top cartilage layer is fixed, the lower cartilage layer is free to rotate. The diagram is not to scale; the synovial fluid region is much thinner than the cartilage regions and can reach molecular scales so that it is effectively squeezed out of the interface. The interfacial conditions for opposing cartilage in shear under such conditions, modelled by homogenized poroviscoelastic media, are derived in this paper together with an examination of select modelling predictions for the resulting mechanics.

in the bulk of the cartilage, away from the interface with the synovial fluid shown in Fig. 1. Note that this figure is not drawn to scale, and that the synovial fluid layer is much thinner than both cartilage layers. The micro lengthscale is representative of the thickness of the synovial fluid. We assume that there is a transition layer between the synovial fluid and the bulk of both layers of cartilage, with thickness of the order of the micro lengthscale, as shown in Fig. 2. Inside these transition layers we will use a microscale model of the cartilage, where a solid scaffold is filled with synovial fluid. A key parameter in Table 1 is the separation of scales parameter ϵ , defined to be the ratio of the micro and macro lengthscales. For the geometries illustrated in Figs 1 and 2 it is clear that, without ambiguity, one of the layers of cartilage modelled may be referred to as the ‘upper poroviscoelastic body’, and the other layer of cartilage as the ‘lower poroviscoelastic body’, with similar remarks applying to the transition layers. Further, the upper poroviscoelastic body is fixed, while the lower poroviscoelastic body is free to move. Where it is necessary to distinguish the upper poroviscoelastic body or transition layer from the lower poroviscoelastic body or transition layer we will use a subscript or superscript $+$ to denote the upper body or layer, and a subscript or superscript $-$ to denote the lower body or layer.

We will write down the macroscale equations for the cartilage in a Lagrangian frame of reference. When deriving the interface conditions we will find it convenient to utilize an Eulerian frame of reference. A subscript 0 is used to denote a region in a Lagrangian frame of reference; regions without this subscript are the corresponding region in an Eulerian frame of reference. When using vectors and tensors we will use an upper case index to denote an index corresponding to a Lagrangian coordinate, and a lower case index to denote an index corresponding to an Eulerian coordinate. We use the summation convention throughout, and also the convention that dimensional quantities are denoted by a superscript asterisk; the corresponding dimensionless quantity has this asterisk removed.

TABLE 1 *The key notation used in this study. Other notation is defined where it is first used. Occasionally there is an overloading of a symbol, such as σ , though the meaning will be clear from context. Dimensional quantities are denoted by a superscript asterisk; quantities without this superscript are the corresponding dimensionless quantity.*

Quantity	Description
d^*	Micro lengthscale
L^*	Macro lengthscale
$\epsilon = d^*/L^*$	Separation of scales parameter; we assume $\epsilon \ll 1$
\mathbf{y}	Microscale Eulerian coordinates
$\mathbf{x} = \epsilon \mathbf{y}$	Macroscale Eulerian coordinates
\mathbf{Y}	Microscale Lagrangian coordinates
$\mathbf{X} = \epsilon \mathbf{Y}$	Macroscale Lagrangian coordinates
\mathbf{F}	Macroscale deformation gradient tensor
\mathbf{G}	Microscale deformation gradient tensor in scaffold
\mathbf{v}	Fluid velocity
\mathbf{V}	Rigid body velocity of the lower poroviscoelastic body
p	Fluid pressure
q	Lagrange multiplier used to enforce incompressibility in scaffold at microscale level
σ	Cauchy stress tensor for the fluid
$\bar{\sigma}$	Cauchy stress tensor for the macroscale poroviscoelastic medium
τ	Cauchy stress tensor for the scaffold
\bar{S}	First Piola–Kirchhoff stress tensor for the scaffold
$\bar{\bar{S}}$	First Piola–Kirchhoff stress tensor for the macroscale poroviscoelastic medium, Excluding swelling and hydrostatic pressures
K	Permeability tensor in the poroviscoelastic body in Eulerian coordinates
\mathbf{N}	Unit normal in Lagrangian coordinates pointing out of lower poroviscoelastic body
Ω_f	The fluid region between the transition layers in Eulerian coordinates
$\Omega_t^{-,+}$	The lower and upper transition layers in Eulerian coordinates
$\Omega_{t,f}^{-,+}$	The fluid region in the lower and upper transition layers in Eulerian coordinates
$\Omega_{t,s}^{-,+}$	The scaffold region in the lower and upper transition layers in Eulerian coordinates
$\partial\Omega_{t,fs}^{-,+}$	Boundary between scaffold and fluid in the transition layers in Eulerian coordinates
$\Omega_{p0}^{-,+}$	The lower and upper poroviscoelastic bodies in Lagrangian coordinates
Λ_0	The interface between the two poroviscoelastic bodies in Lagrangian coordinates
$[g]_{-}^{+}$	Difference of a quantity g between the upper and lower poroviscoelastic bodies

3. The governing equations away from the interface

We model cartilage as a poroviscoelastic body as is common elsewhere; see e.g. [Klika *et al.* \(2016, 2019\)](#) and the references therein. We write down the dimensional equations governing large deformation poroviscoelastic deformations in Section 3.1, and the corresponding dimensionless equations in Section 3.2. One layer of cartilage depicted in Figs 1 and 2 is permitted to move in a manner where the undeformed body is subject to a rigid body transformation. The entries of the strain tensor, and therefore the stress tensor, will be calculated from the tissue deformation relative to a coordinate system that is fixed in the moving undeformed body. To enable us to do this we write down the governing equations in a coordinate system fixed in the moving undeformed body in Section 3.3.

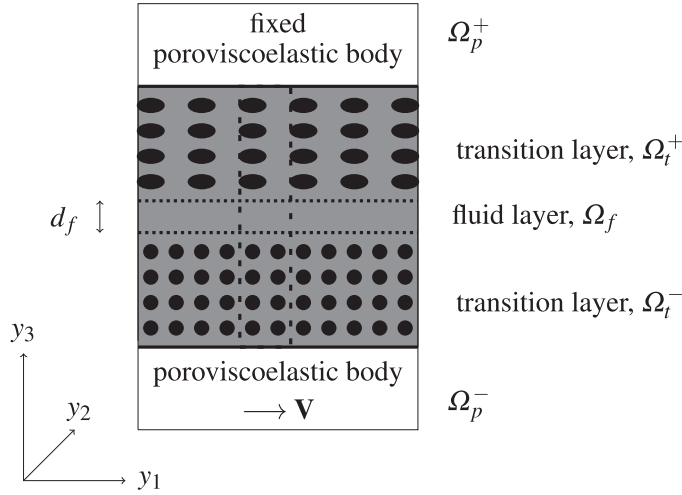


FIG. 2. The geometry of the interface in microscale coordinates. The region bounded by the dashed line is an example of the cell that we homogenize over in Section 5, and the dotted lines delimit the fluid layer from the transition layers.

The two layers of cartilage illustrated in Figs 1 and 2 are separated by a fluid layer that is much thinner than the width of the cartilage. We therefore use macroscale coordinates when writing down the governing equations in Sections 3.1, 3.2 and 3.3 and will use microscale coordinates when writing down a mathematical model of the interface between the layers of cartilage in Section 4. As a consequence, the two layers of cartilage will be adjacent when the interface is written in macroscale coordinates. When writing down conditions that apply across the interface we will require the identification of points in the cartilage layers that are adjacent across the interface; this is discussed in Section 3.4.

3.1 The dimensional governing equations in a fixed poroviscoelastic body

The dimensional governing equations in a poroviscoelastic body occupying the region Ω_{p0}^* in Lagrangian coordinates are Whiteley & Gaffney (2020):

$$\frac{\partial}{\partial X_M^*} \left(\theta_{s,0} \left(\bar{S}_{Mi}^* - F_{Mi}^{-1} \frac{Q^{*2}}{\epsilon_f^*} \right) \right) = J F_{Mi}^{-1} \frac{\partial q^*}{\partial X_M^*}, \quad i = 1, 2, 3, \quad (3.1)$$

$$\frac{\partial J}{\partial t^*} = \frac{\partial}{\partial X_M^*} \left(J F_{Mi}^{-1} K_{ij}^* F_{Nj}^{-1} \frac{\partial q^*}{\partial X_N^*} \right), \quad (3.2)$$

where t^* represents time, $\mathbf{X}^*, \mathbf{x}^*$ are the coordinates of the undeformed and deformed body, $\theta_{s,0}(\mathbf{X}^*)$ is the volume fraction occupied by the solid phase of the poroviscoelastic material in its undeformed state (and is specified), \bar{S}^* is the first Piola–Kirchhoff stress tensor of the poroviscoelastic body without the terms that model hydrostatic pressure or swelling pressure in the fluid within the pores, Q^* is the surface charge density on the scaffold in the poroviscoelastic body, ϵ_f^* is the permittivity of the fluid that fills the pores of the poroviscoelastic body, q^* is a Lagrange multiplier that enforces incompressibility of the scaffold at the microstructure level (and is equal to the fluid pressure in the pores due to both hydrodynamic and swelling pressure), K^* is the permeability tensor of the poroviscoelastic body in

Eulerian coordinates (usually specified by a constitutive relationship), F is the deformation gradient tensor with entries defined by

$$F_{iM} = \frac{\partial x_i^*}{\partial X_M^*}, \quad i, M = 1, 2, 3, \quad (3.3)$$

and $J = \det F$.

We assume the existence of a strain energy density function W^* such that \bar{S}^{e*} , the elastic contribution to \bar{S}^* , has entries given by

$$\bar{S}_{Mi}^{e*} = \frac{\partial W^*}{\partial F_{iM}}, \quad i, M = 1, 2, 3,$$

and that this strain energy function may be decomposed into the sum of volumetric and distortional contributions so that $W^* = W^{v*} + W^{d*}$, allowing us to write

$$\begin{aligned} \bar{S}^{e*} &= \bar{S}^{e,v*} + \bar{S}^{e,d*}, \\ \text{where} \quad \bar{S}_{Mi}^{e,v*} &= \frac{\partial W^{v*}}{\partial F_{iM}}, \quad \bar{S}_{Mi}^{e,d*} = \frac{\partial W^{d*}}{\partial F_{iM}}, \quad i, M = 1, 2, 3, \end{aligned}$$

and $\bar{S}^{e,v*}, \bar{S}^{e,d*}$ represent the volumetric and distortional components of \bar{S}^{e*} .

We assume further that there are N_{relax} viscoelastic relaxation processes with relaxation times τ_γ^* , $\gamma = 1, 2, \dots, N_{\text{relax}}$. Denoting the Cauchy stress tensor by σ^* , we have the relation $J\sigma^* = F\bar{S}^*$. Hence noting $\bar{S}^{e,d*} = JF^{-1}\sigma^{e,d*}$ we have

$$\bar{S}_{Mi}^* = \bar{S}_{Mi}^{e*} + \sum_{\gamma=1}^{N_{\text{relax}}} JF_{Mj}^{-1} Q_{ji}^{\gamma*}, \quad i, M = 1, 2, 3, \quad (3.4)$$

$$\text{where} \quad \frac{DQ_{ji}^{\gamma*}}{Dt^*} + \frac{1}{\tau_\gamma^*} Q_{ji}^{\gamma*} = G_v \frac{D\sigma_{ji}^{e,d*}}{Dt^*}, \quad \gamma = 1, 2, \dots, N_{\text{relax}}, \quad i, j = 1, 2, 3, \quad (3.5)$$

where G_v is a dimensionless scalar, and

$$\frac{D}{Dt^*} = \frac{\partial}{\partial t^*} + V_i^* \frac{\partial}{\partial X_i^*}$$

is the derivative with respect to time in coordinates fixed in the undeformed body moving with velocity V^* . We emphasize the difference between the quantity $Q^{\gamma*}$ used in Eqs. (3.4) and (3.5), and the quantity Q^* that represents the surface charge density on the scaffold. The viscoelastic contributions described by Eqs. (3.4) and (3.5) differ marginally from the approach used in our previous work (Whiteley & Gaffney, 2020) in that the dynamics of relaxation processes are related to the time derivative of the Cauchy stress, rather than the first Piola–Kirchhoff tensor. This ensures the constitutive relation can readily guarantee the symmetry of the Cauchy stress tensor in higher spatial dimensions, whereas such concerns do not arise for the 1D framework of Whiteley & Gaffney (2020).

Using the relationships

$$\frac{\partial J}{\partial F_{iM}} = JF_{Mi}^{-1}, \quad i, M = 1, 2, 3, \quad (3.6)$$

$$\frac{\partial}{\partial X_M^*} (JF_{Mi}^{-1}) = 0, \quad i = 1, 2, 3, \quad (3.7)$$

we may write Eq. (3.1) as

$$\frac{\partial S_{Mi}^*}{\partial X_M^*} = 0, \quad i = 1, 2, 3, \quad (3.8)$$

where

$$S_{Mi}^* = \theta_{s,0} \left(\frac{\partial}{\partial F_{iM}} \left(W^* - \frac{Q^{*2}}{\epsilon_f^*} \log J \right) + \sum_{\gamma=1}^{N_{\text{relax}}} JF_{Mj}^{-1} Q_{ji}^{\gamma*} \right) - JF_{Mi}^{-1} q^*, \quad i, M = 1, 2, 3. \quad (3.9)$$

We now re-write Eq. (3.2) in a form that will be more convenient when modelling two adjacent poroviscoelastic bodies. Using Eqs. (3.6) and (3.7) we may write

$$\begin{aligned} \frac{\partial J}{\partial t^*} &= \frac{\partial J}{\partial F_{iM}} \frac{\partial F_{iM}}{\partial t^*} \\ &= JF_{Mi}^{-1} \frac{\partial}{\partial X_M^*} \left(\frac{\partial x_i^*}{\partial t^*} \right) \\ &= \frac{\partial}{\partial X_M^*} \left(JF_{Mi}^{-1} \frac{\partial x_i^*}{\partial t^*} \right), \end{aligned}$$

allowing us to recast Eq. (3.2) as

$$\frac{\partial}{\partial X_M^*} \left(JF_{Mi}^{-1} \left(\frac{\partial x_i^*}{\partial t^*} - K_{ij}^* F_{Nj}^{-1} \frac{\partial q^*}{\partial X_N^*} \right) \right) = 0. \quad (3.10)$$

Let $\partial\Omega_{p_0}^*$ be the boundary of $\Omega_{p_0}^*$ that does not form part of the interface Λ_0^* between the poroviscoelastic bodies. Suitable boundary conditions for Eq. (3.8) are the specification of \mathbf{x}^* or the applied traction in three orthogonal directions on $\partial\Omega_{p_0}^*$. Suitable boundary conditions for Eq. (3.10) are either specification of q^* , or the flux of fluid per unit undeformed area relative to the (possibly moving) boundary, given by

$$-JF_{Mi}^{-1} K_{ij}^* F_{Nj}^{-1} \frac{\partial q^*}{\partial X_N^*} N_M,$$

where \mathbf{N} is normal to the boundary, of unit magnitude and pointing out of $\Omega_{p_0}^*$. We also require initial conditions for \mathbf{x}^* and $Q_{ji}^{\gamma*}$, $i, j = 1, 2, 3$.

3.2 The dimensionless governing equations in a fixed poroviscoelastic body

We use the nondimensionalization defined by

$$\begin{aligned} \mathbf{X}^* &= L^* \mathbf{X}, & \mathbf{x}^* &= L^* \mathbf{x}, & t^* &= T^* t, & S^* &= \tilde{S}^* S, & W^* &= \tilde{S}^* W, \\ Q^{\gamma*} &= \tilde{S}^* Q^\gamma, & q^* &= \tilde{S}^* q, & K^* &= \bar{K}^* K, & \tau_\gamma^* &= T^* \tau_\gamma, & \mathbf{V}^* &= \frac{L^*}{T^*} \mathbf{V}, \end{aligned} \quad (3.11)$$

where L^* is representative of the macro lengthscale, T^* is representative of the timescale, \tilde{S}^* is representative of the entries of the first Piola–Kirchhoff stress tensor and \bar{K}^* is representative of the entries of the permeability tensor. The dimensionless versions of Eqs. (3.5), (3.8), (3.9) and (3.10) are then, for $\mathbf{X} \in \Omega_{p_0}$:

$$\frac{\partial S_{Mi}}{\partial X_M} = 0, \quad i = 1, 2, 3, \quad (3.12)$$

$$S_{Mi} = \theta_{s,0} \left(\frac{\partial}{\partial F_{iM}} (W - \mathcal{A} \log J) + \sum_{\gamma=1}^{N_{\text{relax}}} J F_{Mj}^{-1} Q_{ji}^\gamma \right) - J F_{Mi}^{-1} q, \quad i, M = 1, 2, 3, \quad (3.13)$$

$$\frac{\partial}{\partial X_M} \left(J F_{Mi}^{-1} \left(\frac{\partial x_i}{\partial t} - \mathcal{B} K_{ij} F_{Nj}^{-1} \frac{\partial q}{\partial X_N} \right) \right) = 0, \quad (3.14)$$

$$\frac{D Q_{ij}^\gamma}{Dt} + \frac{1}{\tau_\gamma} Q_{ij}^\gamma = G_v \frac{D \sigma_{ij}^{e,d}}{Dt}, \quad \gamma = 1, 2, \dots, N_{\text{relax}}, \quad i, j = 1, 2, 3, \quad (3.15)$$

where \mathcal{A}, \mathcal{B} are dimensionless parameters defined by

$$\mathcal{A} = \frac{Q^{*2}}{\epsilon_f^* \tilde{S}^*}, \quad \mathcal{B} = \frac{\bar{K}^* \tilde{S}^* T^*}{L^{*2}}, \quad (3.16)$$

and

$$\frac{D}{Dt} = \frac{\partial}{\partial t} + V_i \frac{\partial}{\partial X_i}.$$

The nondimensionalization defined in this section is also applied to the initial and boundary conditions discussed in Section 3.1.

3.3 The dimensionless governing equations in a moving poroviscoelastic body

Suppose \mathbf{X}, t denote Lagrangian coordinates and time that are fixed in space, and that $\hat{\mathbf{X}}, \hat{t}$ represent Lagrangian coordinates and time fixed in a moving poroviscoelastic body $\hat{\Omega}_{p_0}$. As Lagrangian coordinates represent the undeformed body these coordinate systems are related by a rigid body transformation, i.e. a combination of a rotation and a translation:

$$\hat{X}_N = P_{NM}(t) X_M - R_N(t), \quad N = 1, 2, 3, \quad \hat{t} = t,$$

where $PP^\top = P^\top P = I$, and $\det P = 1$ (Lunn, 1991). Equivalently,

$$X_M = P_{NM}\hat{X}_N + P_{NM}R_N, \quad M = 1, 2, 3, \quad t = \hat{t}. \quad (3.17)$$

Using the chain rule,

$$\frac{\partial}{\partial X_M} = P_{NM} \frac{\partial}{\partial \hat{X}_N}, \quad M = 1, 2, 3, \quad \frac{\partial}{\partial t} = \frac{\partial}{\partial \hat{t}} - V_N \frac{\partial}{\partial \hat{X}_N},$$

where

$$V_N = \dot{R}_N - \dot{P}_{NM}X_M, \quad N = 1, 2, 3,$$

and the dot represents differentiation with respect to t .

The deformed coordinates in the fixed and moving coordinate system, $\mathbf{x}, \hat{\mathbf{x}}$, are also related by

$$x_i = P_{ji}\hat{x}_j + P_{ji}R_j, \quad i = 1, 2, 3, \quad (3.18)$$

giving

$$\frac{\partial x_i}{\partial X_M} = P_{NM} \frac{\partial \hat{x}_j}{\partial \hat{X}_N} P_{ji}, \quad i, M = 1, 2, 3,$$

and so the deformation gradient tensors in the fixed and moving coordinate systems, F, \hat{F} are related by

$$F = P^\top \hat{F} P.$$

The first Piola–Kirchhoff stress, $\boldsymbol{\pi}$, on a surface with unit normal \mathbf{v} has entries

$$\pi_i = S_{Mi}v_M, \quad i = 1, 2, 3,$$

and so $\boldsymbol{\pi} = S^\top \mathbf{v}$. The first Piola–Kirchhoff stress in the moving coordinate system $\hat{\boldsymbol{\pi}}$ is then given by

$$\begin{aligned} \hat{\boldsymbol{\pi}} &= P\boldsymbol{\pi} \\ &= PS^\top P^\top P\mathbf{v} \\ &= \hat{S}^\top \hat{\mathbf{v}}, \end{aligned}$$

where

$$S^\top = P^\top \hat{S}^\top P.$$

Similarly,

$$K = P^\top \hat{K} P, \quad Q^\gamma = P^\top \hat{Q}^\gamma P, \quad \gamma = 1, 2, \dots, N_{\text{relax}}.$$

Noting scalars are frame invariant and using the coordinate system fixed in the moving poroviscoelastic body we may write Eq. (3.14) as

$$\frac{\partial}{\partial \hat{X}_M} \left(J \hat{F}_{Mi}^{-1} \left(\frac{\partial \hat{x}_i}{\partial \hat{t}} - V_N \hat{F}_{iN} + P_{ik} \dot{P}_{jk} (\hat{x}_j + R_j) + \dot{R}_i - \mathcal{B} \hat{K}_{ij} \hat{F}_{Nj}^{-1} \frac{\partial q}{\partial \hat{X}_N} \right) \right) = 0.$$

Noting further that $\frac{\partial}{\partial \hat{X}_M} (J \hat{F}_{Mi}^{-1}) = 0$ for $i = 1, 2, 3$; that $\mathbf{R} = \mathbf{R}(t)$; that $P = P(t)$ is an orthogonal matrix; and that

$$\begin{aligned} \frac{\partial}{\partial \hat{X}_M} (J \hat{F}_{Mi}^{-1} P_{ik} \dot{P}_{jk} \hat{x}_j) &= J \hat{F}_{Mi}^{-1} P_{ik} \dot{P}_{jk} \hat{F}_{jM} \\ &= J P_{ik} \dot{P}_{ik} \\ &= J \frac{d}{dt} \left(\frac{1}{2} P_{ik} P_{ik} \right) \\ &= 0, \end{aligned}$$

Eqs. (3.12)–(3.15) become, for $\hat{\mathbf{X}} \in \hat{\Omega}_{p_0}$:

$$\frac{\partial \hat{S}_{Mi}}{\partial \hat{X}_M} = 0, \quad i = 1, 2, 3, \quad (3.19)$$

$$\hat{S}_{Mi} = \theta_{s,0} \left(\frac{\partial}{\partial \hat{F}_{iM}} (W - \mathcal{A} \log J) + \sum_{\gamma=1}^{N_{\text{relax}}} J \hat{F}_{Mj}^{-1} \hat{Q}_{ji}^{\gamma} \right) - J \hat{F}_{Mi}^{-1} q, \quad i, M = 1, 2, 3, \quad (3.20)$$

$$\frac{\partial}{\partial \hat{X}_M} \left(J \hat{F}_{Mi}^{-1} \left(\frac{\partial \hat{x}_i}{\partial \hat{t}} - V_N \hat{F}_{iN} - \mathcal{B} \hat{K}_{ij} \hat{F}_{Nj}^{-1} \frac{\partial q}{\partial \hat{X}_N} \right) \right) = 0, \quad (3.21)$$

$$\frac{\partial \hat{Q}_{ij}^{\gamma}}{\partial \hat{t}} + \frac{1}{\tau_{\gamma}} \hat{Q}_{ij}^{\gamma} = G_{\gamma} \frac{\partial \hat{\sigma}_{ij}^{e,d}}{\partial \hat{t}}, \quad \gamma = 1, 2, \dots, N_{\text{relax}}, \quad i, j = 1, 2, 3, \quad (3.22)$$

and suitable initial and boundary conditions must also be supplied.

3.4 Locating the interface

As the thickness of the interface is of the order of the microscale coordinate, the two poroviscoelastic bodies are adjacent when the interface Λ_0 is written in macroscale coordinates. To ensure this condition is maintained, the component of the velocity of the two poroviscoelastic bodies in the direction normal to the interface must be equal at the interface:

$$\left[\frac{\partial x_i}{\partial t} n_i \right]_{-}^{+} = 0, \quad (3.23)$$

where \mathbf{n} is a vector of unit magnitude, normal to the interface, pointing out of the lower poroviscoelastic region in Eulerian coordinates, and the notation $[\cdot]_{-}^{+}$ denotes the jump in a quantity from the upper

poroviscoelastic body to the lower poroviscoelastic body. To write Eq. (3.23) in Lagrangian coordinates we use the relationship (e.g. Eqs. (8.17), (8.18) of Gurtin *et al.* (2010)):

$$n_i \, dA = J F_{Mi}^{-1} N_M \, dA_0, \quad i = 1, 2, 3, \quad (3.24)$$

where dA , dA_0 are the elemental surface areas in Eulerian and Lagrangian coordinates, respectively, and we define the Jacobian of the mapping between the undeformed and deformed interface surface, J_A , by

$$J_A = \frac{dA}{dA_0}. \quad (3.25)$$

In Lagrangian coordinates Eq. (3.23) becomes

$$\left[\frac{J}{J_A} F_{Mi}^{-1} \frac{\partial x_i}{\partial t} N_M \right]_{-}^{+} = 0, \quad (3.26)$$

where \mathbf{N} is a vector of unit magnitude, normal to the interface, pointing out of the lower poroviscoelastic region in Lagrangian coordinates. This relationship supplies our first interface condition at the macroscale. We emphasize that the jump in quantities across the interface defined in Eq. (3.26) in Lagrangian coordinates applies to points that are adjacent across the interface in Eulerian coordinates.

To locate points in the deformed upper and lower poroviscoelastic bodies that are adjacent across the interface we consider the Eulerian frame of reference, as this is the frame in which points are physically adjacent. We assume that we know the Lagrangian coordinates of all points on the interface in the poroviscoelastic body that is fixed, i.e. the upper region in Fig. 2. If a point \mathbf{X}^+ in the upper poroviscoelastic body lies on the interface in Lagrangian coordinates then $\mathbf{x}^+(\mathbf{X}^+, t)$ gives the corresponding coordinate in the Eulerian frame at time t . Suppose $\mathbf{Z}(\mathbf{X}^+, t)$ is the Lagrangian coordinate, in a frame fixed in space, of the point on the interface in the lower body that is adjacent to \mathbf{x}^+ in Eulerian coordinates at time t . Then

$$x_i^+(\mathbf{X}^+, t) = x_i^-(\mathbf{Z}(\mathbf{X}^+, t), t), \quad i = 1, 2, 3.$$

Differentiating both sides with respect to t gives, for $i = 1, 2, 3$:

$$\begin{aligned} \frac{\partial x_i^+}{\partial t} &= \frac{\partial x_i^-}{\partial X_M} \frac{\partial Z_M}{\partial t} + \frac{\partial x_i^-}{\partial t} \\ &= F_{iM}^- \frac{\partial Z_M}{\partial t} + \frac{\partial x_i^-}{\partial t}, \end{aligned}$$

where F^- is the deformation gradient tensor evaluated in the lower poroviscoelastic body. As a consequence,

$$\frac{\partial Z_M}{\partial t} = (F^-)^{-1}_{Mi} \left(\frac{\partial x_i^+}{\partial t} - \frac{\partial x_i^-}{\partial t} \right), \quad M = 1, 2, 3. \quad (3.27)$$

Assuming we know the points in the lower poroviscoelastic body that initially lie on the interface, Eq. (3.27) allows us to track the Lagrangian coordinates of points in the lower body that lie on the interface, and the Lagrangian coordinate of the point in the upper body that they are adjacent to.

4. Modelling the interface

We now write down a mathematical model of the interface between two poroviscoelastic bodies that are separated by a thin fluid layer for the case where one poroviscoelastic body is fixed, and the other poroviscoelastic body is free to slide past the fixed body. As discussed in Section 3.4 we assume we know *a priori* the Lagrangian coordinates of points in the fixed body that lie on the interface Λ_0^* , and use Eq. (3.27) to determine the Lagrangian coordinates of the points in the moving body that are adjacent to each point on the fixed body on this interface.

Although we have written down the continuum governing equations for the poroviscoelastic bodies in Lagrangian coordinates, it will be more convenient to use Eulerian coordinates when analysing the equations that apply at interface between the poroviscoelastic bodies. As illustrated in Fig. 2, using microscale Eulerian coordinates, we partition the interface into (i) a thin fluid layer Ω_f^* ; and (ii) transition layers $\Omega_{t,s}^{-,+*}$ between the bulk of both poroviscoelastic regions and the fluid layer, where the transition layers contain both an incompressible solid scaffold component and an incompressible viscous fluid component. A superscript $-$ is used to represent the lower transition layer in Fig. 2, and a superscript $+$ to represent the upper transition layer. We permit the two poroviscoelastic bodies to have different material properties, as illustrated in Figure 2. Theoretical studies on the derivation of the Beavers–Joseph condition for the coupling of Darcy and free fluid flow have found that the thickness of the transition layer is of the same order as the pore lengthscale. We assume that this is also true for the transition layers modelled here and will verify this assumption later. We also assume that (i) the dimensional thickness of the fluid layer, d_f^* , is of the same order as the pore lengthscale; and (ii) the normal to the interface between the poroviscoelastic bodies varies slowly relative to the pore size for the poroviscoelastic bodies. We align the microscale Eulerian coordinate axes so that the normal to the interface between the two poroviscoelastic bodies is in the y_3 direction.

The governing equations in the transition layers are given in Section 4.1, and in the fluid layer in Section 4.2. Boundary conditions where the fluid layer meets the transition layers are given in Section 4.3, and matching conditions between the transition layer and the continuum poroviscoelastic body are given in Section 4.4.

4.1 The transition layers

We will find it convenient to use the variable $\hat{\mathbf{V}}^*$ defined by

$$\hat{\mathbf{V}}^* = \begin{cases} \mathbf{V}^*, & \mathbf{y}^* \in \Omega_t^{-,*}, \\ \mathbf{0}, & \mathbf{y}^* \in \Omega_t^{+,*}, \end{cases} \quad (4.1)$$

so that both undeformed transition layers move with velocity $\hat{\mathbf{V}}^*$. In the transition layers we use Eulerian coordinates and denote the scaffold region by $\Omega_{t,s}^{-,+*}$, the fluid region by $\Omega_{t,f}^{-,+*}$, and the boundary between these regions by $\partial\Omega_{t,fs}^{-,+*}$; the superscripts $-$, $+$ again refer to the lower and upper layers, respectively. We also use the convention, introduced in Section 3.3, that a caret over a coordinate represents a coordinate relative to axes fixed in the undeformed body where the undeformed

body is moving with velocity $\hat{\mathbf{V}}^*$. A mapping $\mathbf{y}^* = \mathbf{y}^*(\mathbf{Y}^*, t^*)$ exists that maps the undeformed scaffold in stationary dimensional microscale Lagrangian coordinates to the deformed scaffold in dimensional microscale Eulerian coordinates. The corresponding map in dimensional microscale Lagrangian coordinates fixed in the moving undeformed body is $\hat{\mathbf{y}}^* = \hat{\mathbf{y}}^*(\hat{\mathbf{Y}}^*, t^*)$. The microscale deformation tensor G and velocity \mathbf{w}^* , relative to stationary Lagrangian coordinates, are then given by

$$\begin{aligned} G_{iM} &= \frac{\partial \hat{y}_i^*}{\partial \hat{Y}_M^*}, \quad i, M = 1, 2, 3, \\ w_i^* &= \frac{\partial y_i^*}{\partial t^*} = \hat{V}_i^* + \frac{\partial \hat{y}_i^*}{\partial t^*}, \quad i = 1, 2, 3. \end{aligned} \quad (4.2)$$

The dimensional equations in the scaffold region are, for $\mathbf{y} \in \Omega_{t,s}^{-,+*}$:

$$\rho_s^* \left(\frac{\partial w_i^*}{\partial t^*} + w_j^* \frac{\partial w_i^*}{\partial y_j^*} \right) = \frac{\partial \tau_{ij}^*}{\partial y_j^*}, \quad i = 1, 2, 3, \quad (4.3)$$

$$\tau_{ij}^* = -q^* \delta_{ij} + \tilde{\tau}_{ij}^*(G, \dot{G}^*, t^*), \quad i, j = 1, 2, 3, \quad (4.4)$$

$$\det G = 1, \quad (4.5)$$

where ρ_s^* is the density of the scaffold, τ^* is the Cauchy stress tensor, $\tilde{\tau}^*$ is the deviatoric Cauchy stress tensor and \dot{G}^* represents the partial derivative of G with respect to time.

The dimensional equations in the fluid region are, for $\mathbf{y} \in \Omega_{t,f}^{-,+*}$:

$$\rho_f^* \left(\frac{\partial v_i^*}{\partial t^*} + v_j^* \frac{\partial v_i^*}{\partial y_j^*} \right) = \frac{\partial \sigma_{ij}^*}{\partial y_j^*}, \quad i = 1, 2, 3, \quad (4.6)$$

$$\sigma_{ij}^* = -p^* \delta_{ij} + \mu_f^* \left(\frac{\partial v_i^*}{\partial y_j^*} + \frac{\partial v_j^*}{\partial y_i^*} \right), \quad i, j = 1, 2, 3, \quad (4.7)$$

$$\frac{\partial v_i^*}{\partial y_i^*} = 0, \quad (4.8)$$

where ρ_f^* is the density of the fluid, \mathbf{v}^* is the dimensional fluid velocity, σ^* is the dimensional Cauchy stress tensor, μ_f^* is the dimensional dynamic viscosity of the fluid and p^* is the dimensional fluid pressure that includes contributions from the swelling pressure due to the Debye layers on the charged scaffold. Note that p^* does not vary at the Debye lengthscale (which is much shorter than the lengthscale modelled by the microscale coordinates \mathbf{y}^*); see Whiteley & Gaffney (2020) for a discussion of this point.

Boundary conditions on $\partial \Omega_{t,fs}^{-,+*}$ are continuity of velocity and stress; for $i = 1, 2, 3$:

$$v_i^* = \hat{V}_i^* + \frac{\partial \hat{y}_i^*}{\partial t^*}, \quad (4.9)$$

$$\left(\tau_{ij}^* - \sigma_{ij}^* + \frac{Q^{*2}}{\epsilon_f^*} \delta_{ij} \right) v_j = 0, \quad (4.10)$$

where \mathbf{v} is the vector of unit magnitude in Eulerian coordinates, normal to $\partial\Omega_{tfs}^{-,+}$, pointing out of the scaffold into the fluid, Q^* is the surface charge density on the scaffold and ϵ_f^* is the permittivity of the fluid. The contribution to Eq. (4.10) from the term that includes Q^{*2}/ϵ_f^* represents the Lorentz force induced by the charged scaffold surface; see [Whiteley & Gaffney \(2020\)](#) for more details on how this term arises. By redefining the pressure p^* by

$$p^* \rightarrow p^* - \frac{Q^{*2}}{\epsilon_f^*}$$

we may absorb the Lorentz force term into the fluid pressure; Eq. (4.10) then becomes

$$\left(\tau_{ij}^* - \sigma_{ij}^* \right) v_j = 0, \quad i = 1, 2, 3. \quad (4.11)$$

We proceed to nondimensionalize, using

$$\begin{aligned} \mathbf{y}^* &= d^* \mathbf{y}, & d_f^* &= d^* d_f, & \mathbf{v}^* &= U^* \mathbf{v}, & \hat{\mathbf{V}}^* &= U^* \hat{\mathbf{V}}, & t^* &= \frac{d^*}{\epsilon U^*} t, \\ \sigma^* &= \frac{\mu_f^* L^* U^*}{d^{*2}} \sigma, & \tau^* &= \frac{\mu_f^* L^* U^*}{d^{*2}} \tau, & p^* &= \frac{\mu_f^* L^* U^*}{d^{*2}} p, & q^* &= \frac{\mu_f^* L^* U^*}{d^{*2}} q, \end{aligned} \quad (4.12)$$

where U^* is representative of the fluid velocity, Eqs. (4.2)–(4.5) become, for $\mathbf{y} \in \Omega_{t,s}^{-,+}$:

$$w_i = \epsilon \frac{\partial y_i}{\partial t} = \hat{V}_i + \epsilon \frac{\partial \hat{y}_i}{\partial t}, \quad i = 1, 2, 3, \quad (4.13)$$

$$\epsilon^3 \frac{\rho_s^*}{\rho_f^*} \text{Re} \left(\epsilon \frac{\partial w_i}{\partial t} + \epsilon w_j \frac{\partial w_i}{\partial y_j} \right) = \frac{\partial \tau_{ij}}{\partial y_j}, \quad i = 1, 2, 3, \quad (4.14)$$

$$\tau_{ij} = -q \delta_{ij} + \hat{\tau}_{ij}, \quad i, j = 1, 2, 3, \quad (4.15)$$

$$\det G = 1, \quad (4.16)$$

where Re is the macroscale Reynolds number, Eqs. (4.6), (4.7) and (4.8) become, for $\mathbf{y} \in \Omega_{t,s}^{-,+}$:

$$\epsilon^2 \text{Re} \left(\epsilon \frac{\partial v_i}{\partial t} + v_j \frac{\partial v_i}{\partial y_j} \right) = \frac{\partial \sigma_{ij}}{\partial y_j}, \quad i = 1, 2, 3, \quad (4.17)$$

$$\sigma_{ij} = -p \delta_{ij} + \epsilon \left(\frac{\partial v_i}{\partial y_j} + \frac{\partial v_j}{\partial y_i} \right), \quad i, j = 1, 2, 3, \quad (4.18)$$

$$\frac{\partial v_i}{\partial y_i} = 0, \quad (4.19)$$

and Eqs. (4.9) and (4.11) become, for $i = 1, 2, 3$ and $\mathbf{y} \in \partial\Omega_{tfs}^{-,+}$:

$$v_i = \hat{V}_i + \epsilon \frac{\partial \hat{y}_i}{\partial t}, \quad (4.20)$$

$$(\tau_{ij} - \sigma_{ij}) v_j = 0. \quad (4.21)$$

We note that to match the solution at the interface with the solution in the continuum poroviscoelastic body we require that the nondimensionalization given by Eq. (4.12) is consistent with that given by Eq. (3.11) for the continuum poroviscoelastic bodies. This will be addressed in Section 5.

4.2 The fluid layer

Using the same notation and nondimensionalization as in Section 4.1, the governing dimensionless equations in fixed Eulerian coordinates in the fluid layer, Ω_f , are, for $\mathbf{y} \in \Omega_f$:

$$\epsilon^2 \text{Re} \left(\epsilon \frac{\partial v_i}{\partial t} + v_j \frac{\partial v_i}{\partial y_j} \right) = \frac{\partial \sigma_{ij}}{\partial y_j}, \quad i = 1, 2, 3, \quad (4.22)$$

$$\sigma_{ij} = -p\delta_{ij} + \epsilon \left(\frac{\partial v_i}{\partial y_j} + \frac{\partial v_j}{\partial y_i} \right), \quad i, j = 1, 2, 3, \quad (4.23)$$

$$\frac{\partial v_i}{\partial y_i} = 0. \quad (4.24)$$

4.3 Boundary conditions where the transition layers meet the fluid

We demand continuity of fluid velocity and stress where the transition layer meets the fluid, i.e. the dotted lines in Fig. 2. This may be written in dimensionless variables as, for $i = 1, 2, 3$:

$$v_i|_- = v_i|_+, \quad (4.25)$$

$$\sigma_{ij}|_- n_j = \sigma_{ij}|_+ n_j, \quad (4.26)$$

where the subscripts $-$, $+$ denote the value of the quantity indicated on either side of this boundary, and \mathbf{n} is the unit vector in Eulerian coordinates, normal to the boundary between the transition layer and the fluid, pointing in the direction from the lower region towards the upper region.

4.4 Matching conditions where the transition layers meet the poroviscoelastic bodies

In Section 5 we will derive macroscale interface conditions by homogenizing the microscale model of the interface using the example cell illustrated in Fig. 2. In this section we write down the matching conditions that are required to couple the two different scales. We observe that the cell shown in Fig. 2 includes upper and lower transition layers with a common periodicity that requires only a very small number of pores. We shall see in Section 5 that the separation of scales parameter $\epsilon = \mathcal{O}(10^{-5})$; this allows us to include a much larger number of pores in the cell we homogenize over while maintaining the condition $\epsilon \ll 1$, giving confidence that a common periodicity exists to a sufficient level of approximation.

The cell we homogenize over is defined by $0 < y_1, y_2 < 1$, $-\infty < y_3 < \infty$, and the scaffold structure is periodic with period 1 in the y_1 and y_2 directions, and \mathcal{P} in the y_3 direction. In Section 5 we will also assume that all solutions are periodic with period 1 in the y_1 and y_2 directions, but will not assume periodicity of the solution in the y_3 direction. We define $\omega(y_3)$ to be the cross-section of the cell at the specified value of y_3 , i.e. the surface $0 < y_1, y_2 < 1$ for a given value of y_3 . In the transition layers, $\omega(y_3) \cap \Omega_{t,s}$ and $\omega(y_3) \cap \Omega_{t,f}$ are the cross-sections of the scaffold and fluid respectively inside the cell that we homogenize over at the specified value of y_3 .

We use an overbar to denote an averaged microscale quantity. In the transition layers the average of any function g in the fluid and scaffold regions is defined by

$$\begin{aligned}\theta_f \bar{g}(\tilde{y}_3) &= \frac{1}{\mathcal{P}} \int_{\tilde{y}_3}^{\tilde{y}_3 + \mathcal{P}} \left(\int_{\omega(y_3) \cap \Omega_{t,f}} g \, dy_1 \, dy_2 \right) dy_3, \\ \theta_s \bar{g}(\tilde{y}_3) &= \frac{1}{\mathcal{P}} \int_{\tilde{y}_3}^{\tilde{y}_3 + \mathcal{P}} \left(\int_{\omega(y_3) \cap \Omega_{t,s}} g \, dy_1 \, dy_2 \right) dy_3.\end{aligned}$$

Note these averaged quantities correspond to a point evaluation for \mathbf{x} dependence of the macroscale model, and also that the volume fractions occupied by the fluid and solid regions, θ_f, θ_s , are given by

$$\theta_f = \frac{1}{\mathcal{P}} \int_{\tilde{y}_3}^{\tilde{y}_3 + \mathcal{P}} \left(\int_{\omega(y_3) \cap \Omega_{t,f}} dy_1 \, dy_2 \right) dy_3, \quad \theta_s = \frac{1}{\mathcal{P}} \int_{\tilde{y}_3}^{\tilde{y}_3 + \mathcal{P}} \left(\int_{\omega(y_3) \cap \Omega_{t,s}} dy_1 \, dy_2 \right) dy_3.$$

By periodicity of the structure of the scaffold in the y_3 direction we see that both θ_f and θ_s are independent of y_3 in both the upper and lower transition layers; where necessary we use superscripts + and - to distinguish the quantities in the upper transition layer from the lower transition layer. The values of θ_f and θ_s in the Eulerian frame are related to the underformed porosity via $\theta_{f,0} = 1 - \theta_{s,0}$ and

$$\theta_s = \frac{\theta_{s,0}}{J}, \quad \theta_f = \frac{J - \theta_{s,0}}{J}.$$

We will also require the average of a function g in the fluid layer. This is defined by

$$\bar{g}(y_3) = \int_{\omega(y_3)} g \, dy_1 \, dy_2. \quad (4.27)$$

We first derive a matching condition for the fluid velocity. Let \mathbf{X} be the Lagrangian coordinates of the point in the fixed, upper body with Eulerian coordinate \mathbf{x} at time t , i.e. $\mathbf{x} = \mathbf{x}(\mathbf{X}, t)$. Then $\mathbf{Z}(\mathbf{X}, t)$ is the Lagrangian coordinates of the point in the moving, lower body with Eulerian coordinate \mathbf{x} at time t , where \mathbf{Z} evolves as described by Eq. (3.27). Using Eq. (4.13), the fluid flux per unit deformed area, \mathcal{F} , in the poroviscoelastic bodies is given by Whiteley & Gaffney (2020):

$$\mathcal{F}_i = \theta_f \left(\hat{V}_i + \epsilon \frac{\partial \hat{y}_i}{\partial t} \right) - \mathcal{B} K_{ij} F_{Mj}^{-1} \frac{\partial q}{\partial X_M}, \quad i = 1, 2, 3.$$

Then, matching the y_3 averaged flux using Eq. (4.27), we have the conditions

$$\lim_{y_3 \rightarrow -\infty} \theta_f \bar{v}_i(\mathbf{y}, t) = \mathcal{F}_i(\mathbf{Z}, t), \quad \lim_{y_3 \rightarrow \infty} \theta_f \bar{v}_i(\mathbf{y}, t) = \mathcal{F}_i(\mathbf{X}, t), \quad i = 1, 2, 3. \quad (4.28)$$

The Eulerian stress in the continuum poroviscoelastic bodies at the interface, \mathcal{E} , is given by

$$\mathcal{E}_i = \frac{1}{J} F_{jM} S_{Mi} n_j, \quad i = 1, 2, 3.$$

Matching the stress at the interface in Eulerian coordinates using Eq. (4.27) gives

$$\lim_{y_3 \rightarrow -\infty} (\theta_f \bar{\sigma}_{ij} + \theta_s \bar{\tau}_{ij}) n_j = \mathcal{E}_i(\mathbf{Z}, t), \quad \lim_{y_3 \rightarrow \infty} (\theta_f \bar{\sigma}_{ij} + \theta_s \bar{\tau}_{ij}) n_j = \mathcal{E}_i(\mathbf{X}, t), \quad i = 1, 2, 3. \quad (4.29)$$

Finally, remembering that the Lorentz force contribution to the stress on the scaffold boundary has been absorbed into the pore pressure in Eq. (4.11) and also the definition of q^* in Section 3.1, we have

$$\lim_{y_3 \rightarrow -\infty} \bar{p} = q(\mathbf{Z}, t), \quad \lim_{y_3 \rightarrow \infty} \bar{p} = q(\mathbf{X}, t), \quad (4.30)$$

where we have averaged p over both the fluid and solid regions, and used the relation $\theta_s + \theta_f = 1$.

5. Multiple scales analysis of the interface

In this section we use asymptotic expansions in the transition and fluid layers to construct leading order interface conditions that may be applied directly to the two continuum poroviscoelastic bodies. For the nondimensionalizations described by Eqs. (3.11) and (4.12) to be consistent, we require that

$$\tilde{S}^* = \frac{\mu_f^* L^* U^*}{d^{*2}}.$$

We set $\tilde{S}^* = E_s^*$, where E_s^* is the Young's modulus of the poroviscoelastic material. Using the parameters given in Table 2 we see that $U^* \approx 10^{-6} \text{ m s}^{-1}$, where U^* is representative of the magnitude of the fluid velocity in the cartilage. In the hip, we would expect that $V^* \approx 0.1 \text{ m s}^{-1}$. As $\epsilon = \mathcal{O}(10^{-5})$, we see that $\mathbf{V} = \mathcal{O}(\epsilon^{-1})$. We also note that the parameters in Table 2 give a macroscale Reynolds number $\text{Re} = \mathcal{O}(\epsilon)$.

We begin by proposing the asymptotic expansions used based on the estimate for V^* above, and defining the framework for a homogenization that uses these asymptotic expansions in Section 5.1, and use these asymptotic expansions to estimate leading order microscale fluid velocity in Section 5.2. We then proceed to demonstrate, in Section 5.3, that the leading order stress on the two poroviscoelastic bodies is unchanged across the interface. In Section 5.4 consideration of the leading order microscale fluid velocity allows us to calculate the leading order stress in directions tangential to the interface. Consideration of the seepage velocity in Section 5.5 velocity then completes the derivation of the interface conditions, which are summarized in Section 5.6.

TABLE 2 *Parameter values for the human hip joint.*

Parameter	Value	Reference or justification
L^*	10^{-3} m	Representative thickness of cartilage layer Hodge <i>et al.</i> (1986)
d^*	6×10^{-9} m	Smaller than surface roughness Katta <i>et al.</i> (2008) ; Mow <i>et al.</i> (1992) , so cartilage effectively directly opposed at macroscale level Ateshian <i>et al.</i> (1994)
Q^*	-0.04 A s m $^{-2}$	Whiteley & Gaffney (2020)
\bar{K}^*	1.72×10^{-15} m 4 N $^{-1}$ s $^{-1}$	DiSilvestro & Francis Suh (2001)
ϵ^*	$78.3 \epsilon_0^*$	Buschmann & Grodzinsky (1995)
ϵ_0^*	8.85×10^{-12} A 2 s 2 N $^{-1}$ m $^{-2}$	Buschmann & Grodzinsky (1995)
ρ_f^*	10^3 kg m $^{-3}$	Knox <i>et al.</i> (1988)
μ_f^*	10^{-2} kg m $^{-1}$ s $^{-1}$	Whiteley & Gaffney (2020)
E_s^*	6.3×10^5 N m $^{-2}$	DiSilvestro & Suh (2001)
τ_γ^*	0.62 s, 7.26 s, 85 s	DiSilvestro & Suh (2001)
G_v	5.32	DiSilvestro & Suh (2001)

5.1 The asymptotic expansions and homogenization framework

We assume that the micro and macro scales may be treated as independent of one another when generating asymptotically valid solutions, as is standard when performing a multiple scales analysis. The micro and macro scale coordinate systems are related by $\mathbf{x} = \epsilon \mathbf{y}$, and so the partial derivatives with respect to the microscale coordinate in the Eulerian frame may be transformed to become

$$\frac{\partial}{\partial y_i} \rightarrow \frac{\partial}{\partial y_i} + \epsilon \frac{\partial}{\partial x_i}, \quad i = 1, 2, 3. \quad (5.1)$$

As the relative velocity between the two poroviscoelastic bodies is $\mathcal{O}(\epsilon^{-1})$ we write

$$V_i = \epsilon^{-1} V_i^{(-1)}, \quad (5.2)$$

where $V_i^{(-1)} = \mathcal{O}(1)$, and propose the following asymptotic expansions for the fluid velocity and fluid pressure in the transition layers and fluid region:

$$v_i = \epsilon^{-1} v_i^{(-1)} + v_i^{(0)} + \epsilon v_i^{(1)} + \dots, \quad i = 1, 2, 3, \quad (5.3)$$

$$p = p^{(0)} + \epsilon p^{(1)} + \epsilon^2 p^{(2)} + \dots \quad (5.4)$$

In the transition layers we write

$$\hat{y}_i = \epsilon^{-1} \hat{x}_i + \hat{y}_i^{(0)} + \epsilon \hat{y}_i^{(1)} + \dots, \quad i = 1, 2, 3, \quad (5.5)$$

$$q = q^{(0)} + \epsilon q^{(1)} + \dots, \quad (5.6)$$

where $\hat{\mathbf{x}}$ is independent of the microscale coordinate. Combining these asymptotic expansions with the transformation of partial derivatives with respect to axes fixed in the undeformed body:

$$\frac{\partial}{\partial \hat{Y}_M} \rightarrow \frac{\partial}{\partial \hat{Y}_M} + \epsilon \frac{\partial}{\partial \hat{X}_M}, \quad M = 1, 2, 3,$$

the microscale deformation gradient tensor G has entries that may be written as a regular asymptotic expansion:

$$G_{iM} = \left(\frac{\partial \hat{x}_i}{\partial \hat{X}_M} + \frac{\partial \hat{y}_i^{(0)}}{\partial \hat{Y}_M} \right) + \epsilon \left(\frac{\partial \hat{y}_i^{(0)}}{\partial \hat{X}_M} + \frac{\partial \hat{y}_i^{(1)}}{\partial \hat{Y}_M} \right) + \dots, \quad i, M = 1, 2, 3.$$

Assuming that $\mathcal{O}(1)$ entries of G and \dot{G} give rise to $\mathcal{O}(1)$ entries in τ , the asymptotic expansions proposed above allow us to write the stress tensors τ and σ as the following regular asymptotic expansions:

$$\tau = \tau^{(0)} + \epsilon \tau^{(1)} + \epsilon^2 \tau^{(2)} + \dots, \quad \sigma = \sigma^{(0)} + \epsilon \sigma^{(1)} + \epsilon^2 \sigma^{(2)} + \dots$$

Noting that

$$\frac{\partial x_i}{\partial t} = \epsilon^{-1} V_i^{(-1)} + \frac{\partial \hat{x}_i}{\partial t} + \epsilon \frac{\partial \hat{y}_i^{(0)}}{\partial t} + \dots,$$

and remembering that we have aligned microscale Eulerian coordinates so that the normal to the interface is in the y_3 direction, the $\mathcal{O}(\epsilon^{-1})$ contribution to Eq. (3.23) allows us to see that our analysis is valid provided

$$V_3^{(-1)} = \mathcal{O}(\epsilon). \quad (5.7)$$

Finally we write the thickness of the fluid layer, d_f as depicted in Fig. 2, via the asymptotic expansion

$$d_f = d_f^{(0)}(\mathbf{X}) + \epsilon d_f^{(1)}(\mathbf{X}, \mathbf{Y}, t) + \epsilon^2 d_f^{(2)}(\mathbf{X}, \mathbf{Y}, t) + \dots, \quad (5.8)$$

where the assumption that the normal to the interface varies slowly relative to the pore size has allowed us to deduce that $d_f^{(0)}$ is independent of \mathbf{Y} . Together with the use of separation distances that are substantially less than surface roughness (see Table 2), this is consistent with reports based on theory that opposing cartilage surface roughness is deformed to allow surface contact given the pressure within a joint (Lin & Klein, 2021).

Furthermore, the nondimensionalization given by Eq. (4.12) has allowed us to deduce that $d_f^{(0)}$ is independent of t . In particular Eqs. (3.23) and (5.7) allow us to deduce that, at leading order, the two transition layers do not undergo relative motion in the y_3 direction.

Media that are porous, poroelastic or poroviscoelastic at the microscale have been homogenized in the past to derive governing equations at the macroscale; see e.g. Burridge & Keller (1981); Collis *et al.* (2017); Holmes (2013); Penta & Gerisch (2018); Penta *et al.* (2014, 2019); Ramírez-Torres *et al.* (2018);

Rohan *et al.* (2016); Whiteley & Gaffney (2020) and the references therein. These studies have all considered microscale and macroscale domains that both have the same number of spatial dimensions, and so the homogenized macroscale governing equations contain quantities that are averaged over all spatial dimensions in the microscale coordinates. When modelling the transition and fluid layers using the coordinate system described in Section 4 and illustrated in Fig. 2, the transition layers and fluid layers have a thickness that is of the order of the microscale coordinates. As a consequence these layers have a thickness that is essentially zero when written in macroscale coordinates. The cell we homogenize over, defined in Section 4.4, occupies the region $0 < y_1, y_2 < 1$, $-\infty < y_3 < \infty$, and we assume periodicity with period 1 in the y_1 and y_2 directions, but not the y_3 direction. Thus, our homogenization differs from that described in the publications cited earlier in this paragraph as we may only upscale in the directions of the microscale coordinates y_1 and y_2 . As a consequence we will not obtain cell problems similar to those that underpin the homogenizations performed by the above-mentioned works. Instead, by taking the limits $y_3 \rightarrow -\infty$, $y_3 \rightarrow \infty$ and using the matching conditions given by Eqs. (4.28)–(4.30), we will see that our approach allows us to derive conditions that relate the macroscale solutions in the upper and lower regions across the interface between the two poroviscoelastic bodies.

5.2 The leading order microscale velocity

We first write down an estimate of the leading order contribution to the microscale velocity which, as we will see later, will allow us to estimate the leading order tangential stress at the interface. As explained earlier, we homogenize over the cell illustrated in Fig. 2, defined by $0 < y_1, y_2 < 1$, $-\infty < y_3 < \infty$, and assume that all solutions are periodic with period 1 in the y_1 and y_2 directions. Substituting the asymptotic expansions given by Eqs. (5.2)–(5.6) into Eqs. (4.17)–(4.19) and (4.22)–(4.24), remembering that $\text{Re} = \mathcal{O}(\epsilon)$, we obtain, at leading order, for $\mathbf{y} \in \Omega_{tf}^{-,+} \cup \Omega_f$:

$$\frac{\partial^2 v_i^{(-1)}}{\partial y_j^2} - \frac{\partial p^{(0)}}{\partial y_i} = 0, \quad i = 1, 2, 3, \quad (5.9)$$

$$\frac{\partial v_i^{(-1)}}{\partial y_i} = 0. \quad (5.10)$$

Boundary conditions are periodicity in the y_1 and y_2 directions, continuity of velocity and stress across the interfaces between the transition layers and fluid layer as given by Eqs. (4.25) and (4.26), and Eq. (4.20) supplies, at leading order, for $i = 1, 2, 3$:

$$v_i^{(-1)} = \begin{cases} V_i^{(-1)}, & \mathbf{y} \in \partial\Omega_{tf}^-, \\ 0 & \mathbf{y} \in \partial\Omega_{tf}^+. \end{cases} \quad (5.11)$$

The matching conditions Eq. (4.28) implies that:

$$\begin{aligned} \theta_f \bar{v}_i^{(-1)} &\rightarrow \theta_f V_i^{(-1)}, & i = 1, 2, 3, & y_3 \rightarrow -\infty, \\ \bar{v}_i^{(-1)} &\rightarrow 0, & i = 1, 2, 3, & y_3 \rightarrow \infty. \end{aligned}$$

However, this is not sufficient to solve for $v_i^{(-1)}$ uniquely as only an average is specified as a boundary condition, and pointwise velocity conditions are required for the uniqueness of Stokes flow solutions up to pressure translations that may depend on the macroscale coordinate \mathbf{x} (Pozrikidis, 1992). We will discuss this point more fully later in this section. However, for matching into the macroscale model, one should not have microscale fluctuations as these cannot be resolved by the macroscale model. Hence we also require the velocity to be the same as its average in the fluid domain and hence we have the conditions

$$v_i^{(-1)} \rightarrow V_i^{(-1)}, \quad i = 1, 2, 3, \quad y_3 \rightarrow -\infty, \quad (5.12)$$

$$v_i^{(-1)} \rightarrow 0, \quad i = 1, 2, 3, \quad y_3 \rightarrow \infty. \quad (5.13)$$

In summary, we see from Eqs. (5.9)–(5.13) that $\mathbf{v}^{(-1)}$ and $p^{(0)}$ satisfy a Stokes flow problem with velocity boundary conditions, where inertial terms are not present in the leading order equations. Some insight to the solution of these equations can be obtained by examining their numerical solution for a simplified geometry that allows the problem to be reduced to two spatial dimensions. By considering only two dimensions we may easily visualize both the leading order velocity components and the leading order pressure, allowing us to highlight features of the solution that will be used when deriving our interface conditions. We claim that these features are also exhibited by the solution on a more realistic three dimensional geometry, and we give independent analytic support for this claim in Appendix A. In particular one objective is to provide evidence that there is no pressure drop across the transition layers, independent of the value of $V_i^{(-1)}$. In addition we will also confirm the legitimacy of our statement in Section 4 that the thickness of the transition layer does not vary in time at leading order.

We thus solve Eqs. (5.9)–(5.13) numerically, with $\mathbf{V}^{(-1)} = (1 \ 0 \ 0)^\top$, so that $\mathbf{v} \rightarrow (1 \ 0 \ 0)^\top$ as $y_3 \rightarrow \infty$. We define a scaffold in both transition layers that has no y_2 dependence, allowing us to deduce that $v_2^{(-1)} = 0$, and also that $v_1^{(-1)}, v_3^{(-1)}, p^{(0)}$ are functions only of y_1 and y_3 . The scaffold in the lower transition layer has ellipsoid cross section with minor axis 0.2 in the y_1 -direction, major axis 0.4 in the y_3 -direction, centred at $y_1 = 0.45, y_3 = -3.5, -2.5, -1.5$. The scaffold in the upper transition layer has ellipsoid cross section with major axis 0.05 in the $(1, 0, 1)^\top$ -direction, minor axis 0.2 in the $(-1, 0, 1)^\top$ -direction, centred at $y_1 = 0.3, 0.8, y_3 = 1.25, 1.75, 2.25$. The quantities $v_1^{(-1)}, v_3^{(-1)}, p^{(0)}$ are plotted in Fig. 3(a), (b), (c), respectively.

A first observation from Fig. 3 is that one assumption made in Section 4, namely that the width of the transition layer is of a lengthscale that is comparable to the pore lengthscale, is valid in this case. There are also other properties of the numerical solutions presented in Fig. 3 that we will find useful in further analysis. First, the solution for $v_1^{(-1)}$ may be approximated by a constant in both transition layers, taking the value 0 in the upper transition layer, and $V_1^{(-1)}$ in the lower transition layer. The solution for $v_1^{(-1)}$ in the fluid layer may then be approximated by a linear function of y_3 that is continuous with the solution in the transition layers. The second observation is that the velocity normal to the interface, $v_3^{(-1)}$, has a much smaller magnitude than $v_1^{(-1)}$, and so can be approximated by zero. The final observation is that there is no pressure difference across the interface layer at leading order, although there are some $\mathcal{O}(1)$ variations in the leading order pressure within the transition layer; this is in contrast to our earlier work on homogenizing a poroviscoelastic body in three dimensions where the leading order pressure is independent of the microscale coordinates (Whiteley & Gaffney, 2020). It should be noted that these variations at the microscale in the leading order pressure decay rapidly as we move away from the

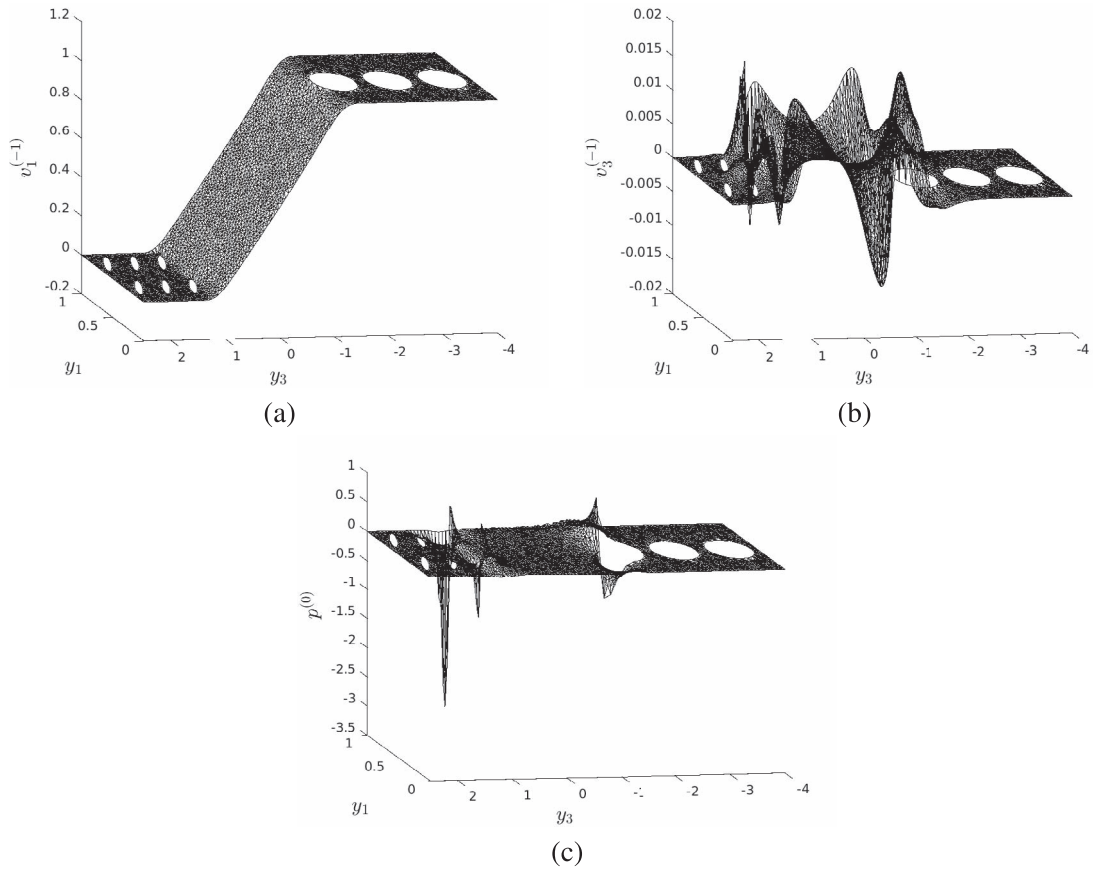


FIG. 3. The numerical solution of Eqs. (5.9)-(5.13) when $\mathbf{V}^{(-1)} = (1 \ 0 \ 0)^\top$.

fluid layer. The first two observations may be combined to deduce that there is a simple shear flow in the centre of the fluid region. We note that, as explained above, these observations are illustrated by the solution of the governing equations using only one highly simplified geometry. The observations were, however, also valid when using different geometries. The interested reader may find an analytic justification for the generality of these observations for more realistic 3D regions in Appendix A, and we assume that they hold for the remainder of this study.

Applying the matching condition given by Eq. (4.30) and the observation that the pressure difference across the interface is zero, we may write

$$q(\mathbf{Z}, t) = q(\mathbf{X}, t),$$

where, as explained in Section 4.4, $\mathbf{Z}(\mathbf{X}, t)$ is the Lagrangian coordinate of the point in the moving, lower body that is adjacent across the interface to the point with Lagrangian coordinate \mathbf{X} on the interface in the fixed, upper body. This allows us to obtain an interface condition, namely continuity of macroscale

pressure across the interface:

$$[q]_-^+ = 0. \quad (5.14)$$

We observed earlier in this section that the leading order pressure determined by Eqs. (5.9)–(5.11) is specified only up to a function of the macroscale coordinate \mathbf{x} , and we note that the interface condition Eq. (5.14) is independent of this function.

5.3 Conservation of stress across the interface

We now demonstrate how conservation of stress allows us to derive three interface conditions that may be applied directly to the two poroviscoelastic bodies. In Section 5.3.1 we derive conservation of stress across the lower transition layer. Similar arguments apply in both the upper transition layer and the fluid layer; an outline of these derivations is given in Sections 5.3.2 and 5.3.3. Combination of the results from Sections 5.3.1, 5.3.2 and 5.3.3 then allows us to deduce conservation of stress across the interface, from which we may deduce interface conditions that may be applied to the poroviscoelastic bodies at the macroscale to be given in Section 5.3.4. Referring back to Fig. 2, in the lower transition layer, we homogenize over the cell defined in microscale Eulerian coordinates by $0 < y_1, y_2 < 1$, $-\infty < y_3 < y_3^-$, in the upper transition layer we homogenize over the cell defined by $0 < y_1, y_2 < 1$, $y_3^+ < y_3 < \infty$, and in the fluid region we homogenize over the cell defined by $0 < y_1, y_2 < 1$, $y_3^- < y_3 < y_3^+$, where all solutions are periodic, with period 1, in the coordinates y_1 and y_2 . The asymptotic expansion for d_f given by Eq. (5.8) allows us to deduce that y_3^- and y_3^+ are constant at leading order and are depicted as dotted lines in Fig. 2.

5.3.1 The lower transition layer. We specify the boundary between the scaffold and fluid regions in the lower transition layer by the level set $\gamma(y_1, y_2, y_3) = 0$, where $\gamma > 0$ in the fluid region and $\gamma < 0$ in the scaffold region. The unit normal vector \mathbf{v} on the boundary between the scaffold and the fluid, pointing out of the scaffold, is then given by

$$\mathbf{v} = \frac{1}{\sqrt{\left(\frac{\partial \gamma}{\partial y_1}\right)^2 + \left(\frac{\partial \gamma}{\partial y_2}\right)^2 + \left(\frac{\partial \gamma}{\partial y_3}\right)^2}} \begin{pmatrix} \frac{\partial \gamma}{\partial y_1} \\ \frac{\partial \gamma}{\partial y_2} \\ \frac{\partial \gamma}{\partial y_3} \end{pmatrix}. \quad (5.15)$$

Recall that we have defined $\omega(y_3)$ to be the cross-section of the cell that we homogenize over at the specified value of y_3 , i.e. the surface $0 < y_1, y_2 < 1$ for a given value of y_3 , and so $\omega(y_3) \cap \Omega_{t,s}$ is the cross-section of the scaffold inside the cell that we homogenize over at the specified value of y_3 . The normal vector to $\omega(y_3) \cap \Omega_{t,s}$, of unit magnitude, pointing out of the scaffold, is given by

$$\mathbf{v}^{2D} = \frac{1}{\sqrt{\left(\frac{\partial \gamma}{\partial y_1}\right)^2 + \left(\frac{\partial \gamma}{\partial y_2}\right)^2}} \begin{pmatrix} \frac{\partial \gamma}{\partial y_1} \\ \frac{\partial \gamma}{\partial y_2} \\ 0 \end{pmatrix}. \quad (5.16)$$

Noting that the derivative of an integral requires us to take account of both the derivative of the integrand and the derivative of the region we are integrating over we have, for $i = 1, 2, 3$:

$$\begin{aligned} \frac{\partial}{\partial y_3} \int_{\omega(y_3) \cap \Omega_{t,s}^-} \tau_{i3}^{(0)} dy_1 dy_2 = \\ \int_{\omega(y_3) \cap \Omega_{t,s}^-} \frac{\partial \tau_{i3}^{(0)}}{\partial y_3} dy_1 dy_2 + \lim_{\delta \rightarrow 0} \frac{1}{\delta} \left(\int_{\omega(y_3 + \delta) \cap \Omega_{t,s}^-} \tau_{i3}^{(0)} dy_1 dy_2 - \int_{\omega(y_3) \cap \Omega_{t,s}^-} \tau_{i3}^{(0)} dy_1 dy_2 \right), \end{aligned}$$

where the limit $\delta \rightarrow 0$ arises from the definition from first principles of the derivative of the region we integrate over. If $\mathbf{y} = (y_1, y_2, y_3)^\top$ lies on $\gamma(y_1, y_2, y_3) = 0$ then, to first order in δ , a Taylor series expansion reveals that the point $\mathbf{y} = (y_1 + \alpha v_1^{2D}, y_2 + \alpha v_2^{2D}, y_3 + \delta)^\top$ also lies on $\gamma(y_1, y_2, y_3) = 0$ for the scalar value of α given by

$$\alpha = - \left(\left(\frac{\partial \gamma}{\partial y_1} \right)^2 + \left(\frac{\partial \gamma}{\partial y_2} \right)^2 \right)^{-1/2} \delta \frac{\partial \gamma}{\partial y_3}.$$

As a consequence, for $i = 1, 2, 3$:

$$\begin{aligned} \lim_{\delta \rightarrow 0} \frac{1}{\delta} \left(\int_{\omega(y_3 + \delta) \cap \Omega_{t,s}^-} \tau_{i3}^{(0)} dy_1 dy_2 - \int_{\omega(y_3) \cap \Omega_{t,s}^-} \tau_{i3}^{(0)} dy_1 dy_2 \right) = \\ - \int_{\omega(y_3) \cap \partial \Omega_{t,s}^-} \left(\left(\frac{\partial \gamma}{\partial y_1} \right)^2 + \left(\frac{\partial \gamma}{\partial y_2} \right)^2 \right)^{-1/2} \tau_{i3}^{(0)} \frac{\partial \gamma}{\partial y_3} ds, \end{aligned}$$

where ds is the arclength element, giving

$$\begin{aligned} \frac{\partial}{\partial y_3} \int_{\omega(y_3) \cap \Omega_{t,s}^-} \tau_{i3}^{(0)} dy_1 dy_2 = \\ \int_{\omega(y_3) \cap \Omega_{t,s}^-} \frac{\partial \tau_{i3}^{(0)}}{\partial y_3} dy_1 dy_2 - \int_{\omega(y_3) \cap \partial \Omega_{t,s}^-} \left(\left(\frac{\partial \gamma}{\partial y_1} \right)^2 + \left(\frac{\partial \gamma}{\partial y_2} \right)^2 \right)^{-1/2} \tau_{i3}^{(0)} \frac{\partial \gamma}{\partial y_3} ds. \quad (5.17) \end{aligned}$$

Integrating the leading order contribution to Eq. (4.14) over $\omega(y_3) \cap \Omega_{t,s}^-$, applying the divergence theorem, and using the expression for \mathbf{v}^{2D} given by Eq. (5.16) yields, for $i = 1, 2, 3$:

$$\begin{aligned} 0 &= \int_{\omega(y_3) \cap \partial\Omega_{t,fs}^-} \tau_{i1}^{(0)} v_1^{2D} + \tau_{i2}^{(0)} v_2^{2D} \, ds + \int_{\omega(y_3) \cap \Omega_{t,s}^-} \frac{\partial \tau_{i3}^{(0)}}{\partial y_3} \, dy_1 \, dy_2 \\ &= \int_{\omega(y_3) \cap \partial\Omega_{t,fs}^-} \left(\left(\frac{\partial \gamma}{\partial y_1} \right)^2 + \left(\frac{\partial \gamma}{\partial y_2} \right)^2 \right)^{-1/2} \left(\tau_{i1}^{(0)} \frac{\partial \gamma}{\partial y_1} + \tau_{i2}^{(0)} \frac{\partial \gamma}{\partial y_2} \right) \, ds + \\ &\quad \int_{\omega(y_3) \cap \Omega_{t,s}^-} \frac{\partial \tau_{i3}^{(0)}}{\partial y_3} \, dy_1 \, dy_2. \end{aligned} \quad (5.18)$$

Combining Eqs. (17) and (5.18) gives, for $i = 1, 2, 3$:

$$\frac{\partial}{\partial y_3} \int_{\omega(y_3) \cap \Omega_{t,s}^-} \tau_{i3}^{(0)} \, dy_1 \, dy_2 = - \int_{\omega(y_3) \cap \partial\Omega_{t,fs}^-} \left(\left(\frac{\partial \gamma}{\partial y_1} \right)^2 + \left(\frac{\partial \gamma}{\partial y_2} \right)^2 \right)^{-1/2} \tau_{ij}^{(0)} \frac{\partial \gamma}{\partial y_j} \, ds. \quad (5.19)$$

We may use a similar argument in the fluid region within the transition layer to that used above, by integrating the leading order contribution to Eq. (4.17) over $\omega(y_3) \cap \Omega_{t,fs}^-$, together with the interface condition Eq. (4.21) to obtain, for $i = 1, 2, 3$:

$$\frac{\partial}{\partial y_3} \int_{\omega(y_3) \cap \Omega_{t,fs}^-} \sigma_{i3}^{(0)} \, dy_1 \, dy_2 = \int_{\omega(y_3) \cap \partial\Omega_{t,fs}^-} \left(\left(\frac{\partial \gamma}{\partial y_1} \right)^2 + \left(\frac{\partial \gamma}{\partial y_2} \right)^2 \right)^{-1/2} \tau_{ij}^{(0)} \frac{\partial \gamma}{\partial y_j} \, ds, \quad (5.20)$$

noting that a potential additional term due to an arclength integral over the external boundary to $\omega(y_3)$,

$$\int_{\partial\omega(y_3)} (\sigma_{i1}^{(0)} n_1^{2D} + \sigma_{i2}^{(0)} n_2^{2D}) \, ds,$$

is zero by periodicity of the unit cell, where \mathbf{n}^{2D} is the outward normal on the external boundary of $\omega(y_3)$.

The leading order Cauchy stress tensor averaged by area over $\omega(y_3)$, $\Sigma_{t,s}^{t,-}$, in the lower transition region is then given by

$$\Sigma_{ij}^{t,-} = \int_{\omega(y_3) \cap \Omega_{t,s}^-} \tau_{ij}^{(0)} \, dy_1 \, dy_2 + \int_{\omega(y_3) \cap \Omega_{t,fs}^-} \sigma_{ij}^{(0)} \, dy_1 \, dy_2, \quad i, j = 1, 2, 3.$$

Combining Eqs. (5.19) and (5.20) we obtain

$$\frac{\partial \Sigma_{i3}^{t,-}}{\partial y_3} = 0, \quad i = 1, 2, 3, \quad -\infty < y_3 < y_3^-, \quad (5.21)$$

and so the macroscale leading order Cauchy stress tensor entries Σ_{i3}^{t-} , $i = 1, 2, 3$ are unchanged across the lower transition layer.

The quantities $\bar{\sigma}$ and $\bar{\tau}$ that are used in the matching condition Eq. (4.29) are defined such that, at leading order and for $i, j = 1, 2, 3$,

$$\begin{aligned}\theta_s \bar{\tau}_{ij}(y_3) + \theta_f \bar{\sigma}_{ij}(y_3) &= \frac{1}{\mathcal{P}} \int_{y_3}^{y_3+\mathcal{P}} \left(\int_{\omega(y_3) \cap \Omega_{ts}^-} \tau_{ij}^{(0)} dy_1 dy_2 + \int_{\omega(y_3) \cap \Omega_{tf}^-} \sigma_{ij}^{(0)} dy_1 dy_2 \right) dy_3 \\ &= \int_{\omega(y_3) \cap \Omega_{ts}^-} \tau_{ij}^{(0)} dy_1 dy_2 + \int_{\omega(y_3) \cap \Omega_{tf}^-} \sigma_{ij}^{(0)} dy_1 dy_2 \\ &= \Sigma_{ij}^{t,-},\end{aligned}\tag{5.22}$$

where the second line follows from the y_3 -independence of the integrand.

5.3.2 The upper transition layer. A similar argument to that used in Section 5.3.1 may be carried out in the upper transition layer. We again define $\omega(y_3)$ to be the surface $0 < y_1, y_2 < 1$ for a given value of $y_3 > y_3^+$. The leading order area weighted Cauchy stress tensor over $\omega(y_3)$, $\Sigma^{t,+}$, in the upper transition layer is given by

$$\Sigma_{ij}^{t,+} = \int_{\omega(y_3) \cap \Omega_{ts}^+} \tau_{ij}^{(0)} dy_1 dy_2 + \int_{\omega(y_3) \cap \Omega_{tf}^+} \sigma_{ij}^{(0)} dy_1 dy_2, \quad i, j = 1, 2, 3,$$

allowing us to obtain the analogous equations to Eq. (5.21) and (5.22) in the upper transition layer:

$$\Sigma_{ij}^{t,+} = \theta_s \bar{\tau}_{ij}(y_3) + \theta_f \bar{\sigma}_{ij}(y_3), \quad \frac{\partial \Sigma_{i3}^{t,+}}{\partial y_3} = 0, \quad i = 1, 2, 3, \quad y_3^+ < y_3 < \infty.\tag{5.23}$$

5.3.3 The fluid layer. We define Σ^f to be the $\mathcal{O}(1)$ area weighted Cauchy stress tensor for a given value of y_3 in the fluid layer:

$$\Sigma_{ij}^f(y_3) = \int_{\omega(y_3)} \sigma_{ij}^{(0)}(\mathbf{y}) dy_1 dy_2, \quad i, j = 1, 2, 3.$$

Integrating the leading order contribution to Eq. (4.22), applying the divergence theorem and periodicity we obtain

$$\frac{\partial \Sigma_{i3}^f}{\partial y_3} = 0, \quad i = 1, 2, 3, \quad y_3^- < y_3 < y_3^+.\tag{5.24}$$

5.3.4 *Macroscale stress continuity interface conditions.* We may upscale Eq. (4.26) at $y_3 = y_3^-, y_3^+$ to macroscale coordinates yielding, for $i = 1, 2, 3$:

$$\begin{aligned}\Sigma_{i3}^{t,-} &= \Sigma_{i3}^f, & y_3 &= y_3^-, \\ \Sigma_{i3}^{t,+} &= \Sigma_{i3}^f, & y_3 &= y_3^+.\end{aligned}$$

Eqs. (5.21), (5.23), (5.24) then imply

$$\lim_{y_3 \rightarrow -\infty} \Sigma_{3i}^{t,-} = \lim_{y_3 \rightarrow -\infty} \Sigma_{ji}^{t,-} n_j = \lim_{y_3 \rightarrow \infty} \Sigma_{3i}^{t,+} = \lim_{y_3 \rightarrow \infty} \Sigma_{ji}^{t,+} n_j, \quad i = 1, 2, 3, \quad (5.25)$$

using the assumption that the unit normal, which points out of the lower poroviscoelastic region, varies slowly relative to the pore size and thus can be taken to be a constant unit vector in the increasing y_3 direction.

To write Eq. (5.25) in Lagrangian coordinates we use Eqs. (3.24), (4.29) and the relationship $J\Sigma = FS$ to give conservation of stress in Lagrangian coordinates at the macroscale level across the interface:

$$\left[\frac{1}{J_A} S_{Mi} N_M \right]_{-}^{+} = 0, \quad i = 1, 2, 3, \quad (5.26)$$

supplying three interface conditions that may be applied directly to the poroviscoelastic bodies. As would be expected, this interface condition depends on the stress tensor of the homogenized bodies away from the interface, rather than the stress tensors of the scaffold and fluid that appear in the model of the interface and fluid layers at the microscale.

5.4 The shear stress at the interface

Three interface conditions that may be applied to the macroscale poroviscoelastic bodies are given by Eq. (5.26). In this section we use consideration of the microscale fluid velocity to derive expressions for the shear stress that provide two more equations that may be applied at the interface.

In Section 5.3 we deduced that the averaged microscale leading order stress was independent of the coordinate y_3 . We may therefore estimate this stress in the fluid region, as the absence of a scaffold component makes this region the simplest region in which to estimate the stress. Noting that Eq. (5.8) implies that $d_f = y_3^+ - y_3^-$ is a function only of \mathbf{X} at leading order, we see from the observations of the numerical solutions plotted in Fig. 3 and Eqs. (4.18), (5.3), (5.8) that, to excellent approximation, two further interface conditions are

$$\Sigma_{31}^{tf} = -\frac{V_1^{(-1)}}{d_f^0}, \quad \Sigma_{32}^{tf} = -\frac{V_2^{(-1)}}{d_f^0}. \quad (5.27)$$

Further analytical support for Eq. (5.27) is provided in Appendix A, where it is shown that Σ_{31}^{tf} is constant at leading order for transition regions with a reflection symmetry, and this would trivially generalize for Σ_{32}^{tf} when $V_2^{(-1)} \neq 0$.

Remembering that the axes in Eulerian coordinates have been aligned so that $\mathbf{n} = (0 \ 0 \ 1)^\top$, we may define $\mathbf{t}^1 = (1 \ 0 \ 0)^\top$, $\mathbf{t}^2 = (0 \ 1 \ 0)^\top$ to be two tangent vectors in Eulerian coordinates. Using

Eq. (3.24) we may write, for $i = 1, 2$:

$$\begin{aligned}\Sigma_{3i}^{tf} &= n_j \Sigma_{jk} t_k^i \\ &= \frac{1}{J_\Lambda} N_M S_{Mj} t_j^i,\end{aligned}$$

allowing us to write

$$S_{Mj} N_M t_j^1 = -\frac{J_\Lambda V_1^{(-1)}}{d_f^0}, \quad S_{Mj} N_M t_j^2 = -\frac{J_\Lambda V_2^{(-1)}}{d_f^0}. \quad (5.28)$$

providing a further two interface conditions in Lagrangian coordinates.

5.5 The leading order seepage velocity

Remembering that $v_i^{(-1)}$ is observed to be constant to excellent approximation in the lower transition layer for the numerical solutions plotted in Fig. 3, the $\mathcal{O}(1)$ contribution to Eqs. (4.19) and (4.20) supply

$$\frac{\partial v_i^{(0)}}{\partial y_i} = 0, \quad \mathbf{y} \in \Omega_{tf}^-, \quad (5.29)$$

$$v_i^{(0)} = \frac{\partial x_i}{\partial t}, \quad \mathbf{y} \in \partial \Omega_{tfs}^-, \quad i = 1, 2, 3. \quad (5.30)$$

We define \tilde{v}_3^0 by

$$\tilde{v}_3^{(0)} = \int_{\omega(y_3) \cap \Omega_{tfs}^-} v_3^{(0)} \, dy_1 \, dy_2. \quad (5.31)$$

Note that this is a different averaging to Eq. (4.27), hence use of a tilde rather than an overbar. Using similar arguments to those used to derive Eqs. (5.19) and (5.20), and the definition of \mathbf{v} given by Eq. (5.15), we obtain

$$\frac{\partial \tilde{v}_3^{(0)}}{\partial y_3} = \int_{\omega(y_3) \cap \partial \Omega_{tfs}^-} v_i^{(0)} v_i \frac{(\gamma_{y_1}^2 + \gamma_{y_2}^2 + \gamma_{y_3}^2)^{1/2}}{(\gamma_{y_1}^2 + \gamma_{y_2}^2)^{1/2}} \, ds,$$

where ds is the arclength element and, for brevity, subscripts are used to denote partial derivatives of γ . Integrating over the interval $y_3' < y_3 < y_3''$ gives

$$\tilde{v}_3^{(0)}(y_3'') - \tilde{v}_3^{(0)}(y_3') = \int_{y_3'}^{y_3''} \int_{\omega(y_3) \cap \partial \Omega_{tfs}^-} v_i^{(0)} v_i \frac{(\gamma_{y_1}^2 + \gamma_{y_2}^2 + \gamma_{y_3}^2)^{1/2}}{(\gamma_{y_1}^2 + \gamma_{y_2}^2)^{1/2}} \, ds \, dy_3. \quad (5.32)$$

Parameterizing the position vector of points on this surface via $\mathbf{r}(y_3, s)$, the surface area element of the inclusion is given by

$$\begin{aligned} dS &= \left| \frac{\partial \mathbf{r}}{\partial s} \wedge \frac{\partial \mathbf{r}}{\partial y_3} \right| ds dy_3 \\ &= \left| \frac{\partial \mathbf{r}}{\partial s} \right| \left| \frac{\partial \mathbf{r}}{\partial y_3} \right| ds dy_3 \\ &= \left| \begin{pmatrix} -\gamma_{y_1} \gamma_{y_3} / (\gamma_{y_1}^2 + \gamma_{y_2}^2) \\ -\gamma_{y_2} \gamma_{y_3} / (\gamma_{y_1}^2 + \gamma_{y_2}^2) \\ 1 \end{pmatrix} \right| ds dy_3 \\ &= \frac{(\gamma_{y_1}^2 + \gamma_{y_2}^2 + \gamma_{y_3}^2)^{1/2}}{(\gamma_{y_1}^2 + \gamma_{y_2}^2)^{1/2}} ds dy_3, \end{aligned}$$

where we have used $|\partial \mathbf{r} / \partial s| = 1$, which is immediate from the definition of arclength. Hence, noting $\mathbf{v}^{(0)} = \partial \mathbf{x} / \partial t$ on the scaffold inclusion surface with \mathbf{x} independent of the microscale coordinates, and using Eq. (5.32), we have

$$\begin{aligned} \tilde{v}_3^{(0)}(y_3'') - \tilde{v}_3^{(0)}(y_3') &= \frac{\partial x_i}{\partial t} \int_{y_3'}^{y_3''} \int_{\omega(y_3) \cap \partial \Omega_{t,fs}^-} v_i dS \\ &= 0, \end{aligned} \tag{5.33}$$

where the final equality is given by the divergence theorem, and so $\tilde{v}_3^{(0)}$ is independent of y_3 . Using Eqs. (4.27) and (5.31) we see that

$$\theta_f \bar{v}_3(y_3) = \frac{1}{\mathcal{D}} \int_{y_3}^{y_3^* + \mathcal{D}} \tilde{v}_3^{(0)} dy_3,$$

from which we may use the y_3 independence of $\tilde{v}_3^{(0)}$ to deduce that

$$\frac{\partial}{\partial y_3} (\theta_f \bar{v}_3) = 0,$$

and it follows that

$$\frac{\partial}{\partial y_3} \left(\theta_f \left(\bar{v}_3 - \frac{\partial x_3}{\partial t} \right) \right) = 0.$$

The corresponding result in the upper transition layer follows from a similar argument. In the fluid region, integrating Eq. (4.24) over the region $0 < y_1, y_2 < 1$, applying the divergence theorem in the plane, invoking periodicity, and remembering that the fluid region is moving with velocity $\partial x_3 / \partial t$ in the

y_3 direction allows us to deduce that

$$\theta_f^- \left(\bar{v}_3^- - \frac{\partial x_3}{\partial t} \right) = \theta_f^+ \left(\bar{v}_3^+ - \frac{\partial x_3}{\partial t} \right). \quad (5.34)$$

Combining the results from Eqs. (5.33) and (5.34) allows us to deduce that

$$\lim_{y_3 \rightarrow -\infty} \theta_f^- \left(\bar{v}_3^- - \frac{\partial x_3}{\partial t} \right) = \lim_{y_3 \rightarrow \infty} \theta_f^+ \left(\bar{v}_3^+ - \frac{\partial x_3}{\partial t} \right).$$

Application of the matching condition given by Eq. (4.28) then allows us to deduce that the pressure driven flux of fluid normal to the interface is conserved across the interface:

$$\left[\mathcal{B} K_{ij} F_{Nj}^{-1} \frac{\partial q}{\partial X_N} n_i \right]_-^+ = 0,$$

which, using Eq. (3.24), may be written in Lagrangian coordinates as

$$\left[\frac{J}{J_\Lambda} \mathcal{B} F_{Mi}^{-1} K_{ij} F_{Nj}^{-1} \frac{\partial q}{\partial X_N} N_M \right]_-^+ = 0. \quad (5.35)$$

5.6 Interface conditions for the macroscale problem

On the boundary of a poroviscoelastic body we would expect to apply four boundary conditions. Three of these would be displacement or applied stress in three orthogonal directions. The final condition would be the specification of fluid flux normal to the boundary (a Neumann boundary condition for the Darcy equation) or the pore pressure (a Dirichlet boundary condition for the Darcy equation). At the interface between two poroviscoelastic bodies we would expect twice the number of boundary conditions usually prescribed. Based on the earlier analysis suitable boundary conditions are, at leading order:

$$\text{Eq. (3.26) :} \quad \left[\frac{J}{J_\Lambda} F_{Mi}^{-1} \frac{\partial x_i}{\partial t} N_M \right]_-^+ = 0, \quad (5.36)$$

$$\text{Eq. (5.26) :} \quad \left[\frac{1}{J_\Lambda} S_{Mi} N_M \right]_-^+ = 0, \quad i = 1, 2, 3, \quad (5.37)$$

$$\text{Eq. (5.28) :} \quad \frac{1}{J_\Lambda} S_{Mj} N_M t_j^i = - \frac{V_i^{(-1)}}{d_f}, \quad i = 1, 2, \quad (5.38)$$

$$\text{Eq. (5.14) :} \quad [q]_-^+ = 0, \quad (5.39)$$

$$\text{Eq. (5.35) :} \quad \left[\frac{J}{J_\Lambda} \mathcal{B} F_{Mi}^{-1} K_{ij} F_{Nj}^{-1} \frac{\partial q}{\partial X_N} N_M \right]_-^+ = 0. \quad (5.40)$$

The eight interface conditions given by Eqs. (5.36)–(5.40) are of the form expected. Eqs. (5.37) and (5.38) provide two stress boundary conditions in both tangential expressions, and Eqs. (5.36) and (5.37)

provide one displacement and one stress boundary condition in the normal direction. Eq. (5.39) specifies the pore pressure difference across the interface, and Eq. (5.40) confirms that the fluid flux across the interface is continuous in the direction normal to the interface.

6. Numerical simulations

We now present some exemplar numerical simulations in two spatial dimensions to illustrate the application of the interface conditions derived in Section 5. We use a very simple model of the knee joint, comprising an upper layer of poroviscoelastic material sliding over a fixed lower layer of poroviscoelastic material with a prescribed speed. The conclusions of Maroudas *et al.* (1968) suggest that the lower boundary of the lower layer and the upper boundary of the upper layer should be modelled as being impermeable for mature cartilage, and permeable for immature cartilage that is seen in young children; we consider these cases separately.

6.1 Mature cartilage

For mature cartilage we model a lower layer of cartilage occupying the region $0 < X_1^* < 0.08$ m, $0 < X_2^* < 0.001$ m in Lagrangian coordinates, and an upper layer of cartilage occupying the region $0 < X_1^* < 0.08$ m, 0.001 m $< X_2^* < 0.002$ m in Lagrangian coordinates. Zero displacement boundary conditions in both directions are applied on the lower boundary $X_2^* = 0$. Zero displacement in the X_1^* direction relative to the moving undeformed body is applied on the top boundary of the upper layer $X_2^* = 0.002$ m, together with a downward force T^* per unit undeformed area in the negative X_2^* direction, where T^* is of magnitude

$$T^* = \left(A^* - B^* \cos \frac{2\pi X_1^*}{L_x^*} \right) (1 - e^{-t^*}), \quad (6.1)$$

where $L_x^* = 0.08$ m and t^* is in units s. The profile shown in Brown & Shaw (1984) suggests $A^* = 2 \times 10^6$ N m⁻² and $B^* = 1.5 \times 10^6$ N m⁻² as representative values for knee cartilage that give realistic stresses for t^* (measured in units of s) sufficiently large. Periodic boundary conditions are applied at $X_1^* = 0, L_x^*$. As explained above, the lower and upper boundaries are modelled as impermeable (Maroudas *et al.*, 1968). Unless otherwise stated we use the parameters given in Table 2, together with a Poisson's ratio of 0.1 (DiSilvestro & Suh, 2001), and $\theta_{s,0} = 0.3$, representative of the values used in Whiteley & Gaffney (2020). A Young's modulus $E_s^* = 7 \times 10^6$ N m⁻², representative of knee cartilage (Shepherd & Seedhom, 1999), was used. For consistency with the value of V^* given in Section 5 we set

$$\mathbf{V}^* = (0.1 \sin 2\pi t^*, 0)^\top, \quad (6.2)$$

where the non-zero component of \mathbf{V}^* is in units m s⁻¹, and t^* is in units s. Initial displacement at $t^* = 0$ is compatible with Eq. (6.1), and so the initial displacement is due only to the swelling of the undeformed body. All viscoelastic contributions to the stress tensor are initially zero. Elastic contributions to the stress tensor, i.e. the contributions that are not due to the hydrodynamic pressure, the swelling pressure or viscoelasticity are those used in Whiteley & Gaffney (2020):

$$\theta_{s,0} S_{Mi}^* = \mu^* \left(F_{iM} - J F_{Mi}^{-1} \right) + \frac{3\lambda^* + 2\mu^*}{3} J(J-1) F_{Mi}^{-1}, \quad i, M = 1, 2, \quad (6.3)$$

where λ^* , μ^* are the Lamé constants. We may write the dimensional version of Eq. (5.38) as

$$S_{Mj}^* N_{Mtj} = -\alpha V J_A E_s^*, \quad (6.4)$$

where V is the magnitude of the dimensionless velocity corresponding to Eq. (6.2). In the absence of any experimental data to guide the choice of α we will present simulations where $\alpha = 0, 0.005, 0.01, 0.015$. The non-zero values of α correspond to separations between the lower and upper cartilage regions of 2.8×10^{-8} m, 1.4×10^{-8} m, 9.5×10^{-9} m.

Numerical solutions are calculated using the finite element method. Following [Chen *et al.* \(2020\)](#); [Murad & Loula \(1994\)](#), on each element we use a tensor product quadrilateral approximation to the coordinates of the deformed body, and a tensor product linear approximation to the pore pressure. All time derivatives are evaluated implicitly. The interface conditions given in Section 5.6 are implemented using the method of Lagrange multipliers in a similar manner to that used for fluid-solid interaction problems; see e.g. [Nordsletten *et al.* \(2010\)](#).

The deformation of the cartilage from an initially uniform grid is shown in Fig. 4 at two points in the loading cycle for the case where $\alpha = 0.01$. In this figure lines that are almost vertical represent lines that are vertical in the undeformed body, and lines that are almost horizontal represent lines that are horizontal in the undeformed body. The thicker line represents the interface between the two layers of cartilage. In Fig. 4(a) we plot the deformation at time $t^* = 100$ s, where the velocity given by Eq. (6.2) has zero magnitude. The interface condition Eq. (5.38) therefore enforces zero tangential stress between the two layers, and the compressive force given by Eq. (6.1) is the only external force applied to the cartilage. In Fig. 4(b) the deformed cartilage region is plotted at time $t^* = 100.25$ s, where the velocity given by Eq. (6.2)—and therefore the tangential stress between the two layers of cartilage—takes its maximum magnitude, and so the cartilage is subjected to an additional shear force between the cartilage layers in addition to the compressive force. This additional tangential stress may be seen by noting that the lines that are almost vertical have a slightly larger deflection away from the vertical in Fig. 4(b) than in Fig. 4(a). We note that there is very little X_1^* dependence on the solution, despite the X_1^* dependence on the boundary condition given by Eq. (6.1).

In Fig. 5 we illustrate the effect of α , and thus the fluid layer thickness, on the maximum eigenvalue of the Cauchy stress tensor, σ_{\max}^* , as a function of time. In this figure the solid line represents $\alpha = 0.015$, the broken line represents $\alpha = 0.01$, the dash-dotted line represents $\alpha = 0.005$, and the dotted line represents $\alpha = 0$. Some observations from Fig. 5 confirm properties that would be expected from Eq. (6.4). First, σ_{\max}^* is largest for non-zero α when V takes its largest value. Furthermore, the maximum value of σ_{\max}^* increases as α increases. Finally, the values of σ_{\max}^* when $V = 0$ are only very weakly dependent on α .

6.2 Immature cartilage

As pointed out at the start of Section 6 immature cartilage may be modelled as having a porous boundary ([Maroudas *et al.*, 1968](#)), in contrast to the boundary conditions used in Section 6.1. In addition, in a crude attempt to modify the mature cartilage parameters used in Section 6.1 so as to be suitable for simulating immature cartilage, we reduce the spatial dimensions given in Section 6.1 by a factor of 2, the constants A^* , B^* given in Eq. (6.1) by a factor of 4, and set $\alpha = 0.005$.

The deformed cartilage is shown in Fig. 6 at the same times as that shown in Section 6.1. Note that, in common with mature cartilage, there is more of a deflection when the magnitude of V is largest. In contrast to mature cartilage simulated in Fig. 4 we see that there is more X_1^* dependence in the solution,

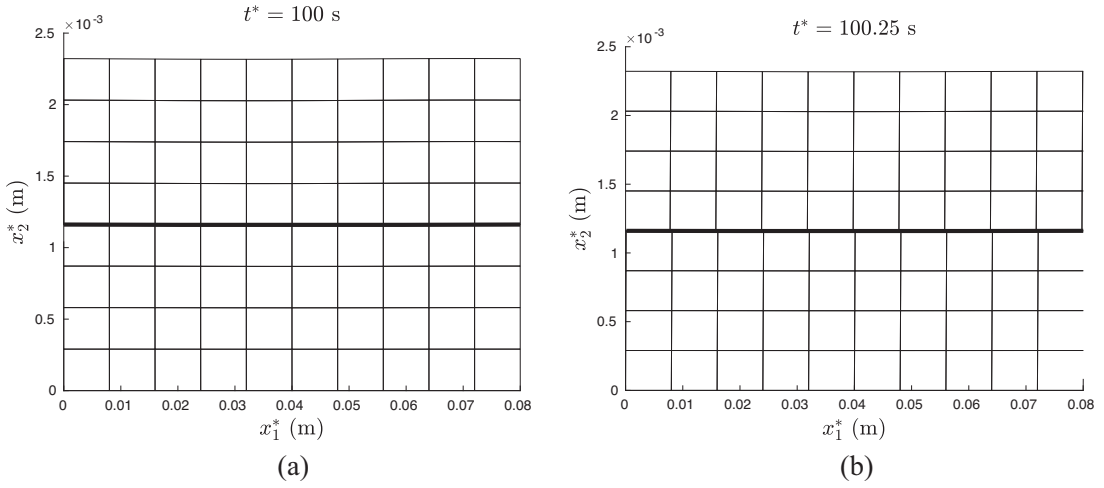


FIG. 4. (a) Deformed mature cartilage at time $t^* = 100$ s (where the translational velocity is zero). (b) Deformed mature cartilage at time $t^* = 100.25$ s (where the translational velocity takes its maximum value). The parameter values for both plots are discussed in the main text, with $\alpha = 0.01$ and other parameters taken from Table 2. Lines that are almost vertical represent lines that are vertical in the undeformed body, and lines that are almost horizontal represent lines that are horizontal in the undeformed body. The thicker line represents the interface between the two layers of cartilage.

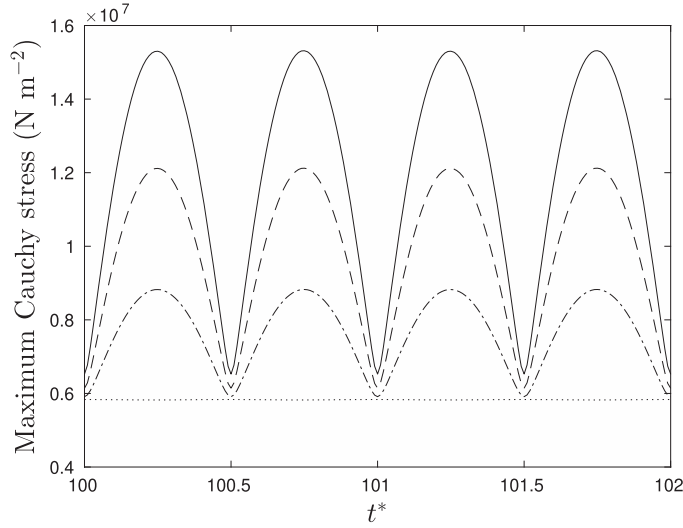


FIG. 5. The effect of varying α on σ_{\max}^* for the mature cartilage simulations, with all other parameters as in Fig. 4. The solid line represents $\alpha = 0.015$, the broken line represents $\alpha = 0.01$, the dash-dotted line represents $\alpha = 0.005$, the dotted line represents $\alpha = 0$.

although this is not particularly pronounced. In Fig. 7 we plot the maximum eigenvalue of the Cauchy stress tensor, σ_{\max}^* , as a function of time. We see similar features to those discussed in Section 6.1 for mature cartilage.

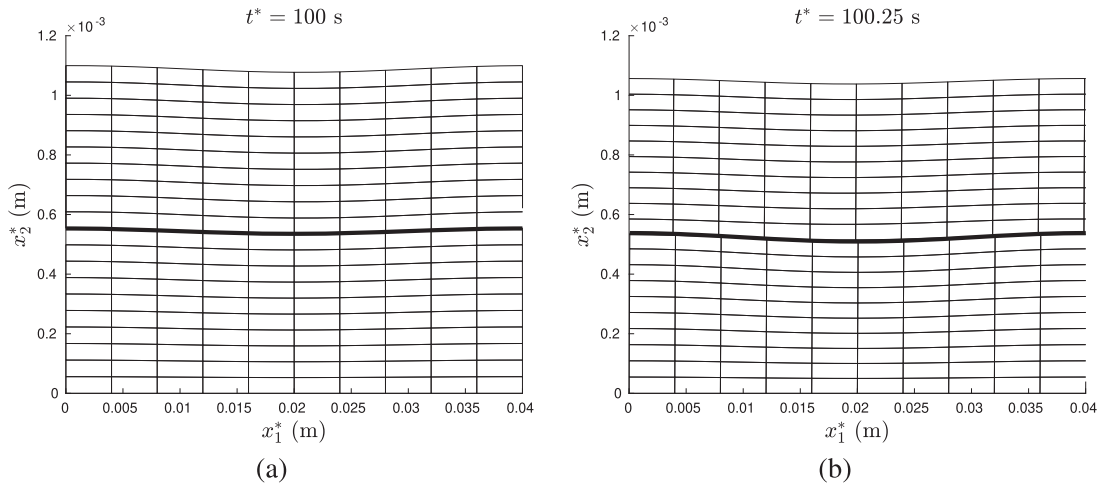


FIG. 6. (a) Deformed immature cartilage at time $t^* = 100$ s (where the translational velocity is zero). (b) Deformed immature cartilage at time $t^* = 100.25$ s (where the translational velocity takes its maximum value). Lines that are almost vertical represent lines that are vertical in the undeformed body, and lines that are almost horizontal represent lines that are horizontal in the undeformed body. The thicker line represents the interface between the two layers of cartilage.

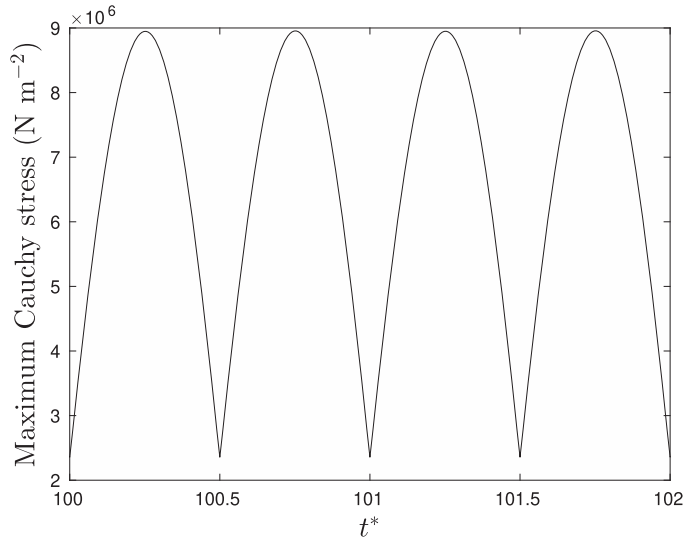


FIG. 7. σ_{\max}^* as a function of time for the immature cartilage simulations. in Eq. (6.4).

7. Discussion and conclusions

In this paper we have used a homogenization asymptotic analysis based on a separation of lengthscales between the poresize and the macroscale to derive interface conditions for two adjacent poroviscoelastic layers. These layers are under load and separated by a fluid layer which is very thin, as depicted in Fig. 2,

and contain a Newtonian interstitial fluid together with a fixed charge density attached to a solid scaffold that is represented by finite deformation viscoelasticity.

The derived interface conditions for this system use properties of the pore-scale Stokes problem associated with the flow of fluid within the solid scaffold and the separating layer. This is, to good approximation, a simple shear flow between the poroviscoelastic layers above and below the interface, together with constant flow matching that of the scaffold in the poroviscoelastic medium in each layer. Determining this flow analytically would be prohibitive given the lack of simplifying continuous symmetries and the multiply connected domains; e.g. singularity methods would generate an essentially intractable image system, while conformal mapping methods still require numerical schemes even for much simpler 2D problems (Luca & Crowdy, 2018). Hence the nature of the flow within the solid scaffold and the separating layer has been demonstrated numerically in the main text, with an analysis demonstrating shear flow in the Appendix to good approximation, even in fully 3D problems, without the need to solve the equations exactly. In particular, when the upper and lower layers have the same scaffold, the only feature of the interfacial conditions not explicitly determined by analysis is the fluid layer shear flow strength, that is the dimensional right hand side of interface condition Eq. (5.38), $-\mu_f^* V^*/d_f^*$, where μ_f^* is the dynamic viscosity of the fluid, V^* is the relative tangential speed between the two layers, and d_f^* is the separation of the layers. The numerical solution of the pore-scale Stokes problem in the main text demonstrates this is the appropriate term in Eq. (5.38), which also generalizes the Beavers–Joseph condition for fluid shear adjacent to a porous medium to the shear of two adjacent poroviscoelastic layers sliding past each other, separated by a fluid layer.

Further general results using the asymptotic analysis demonstrate that d_f^* , the separation of the layers, is not spatially dependent on the pore scale at leading order, although variation at the macroscale can occur. Noting that d_f^* in this study can be taken to be much smaller than the micro scale of surface roughness and down to the scale of the pore size, the observation of constant pore-scale d_f^* is not inconsistent with recent computational studies reporting that the surface roughness of cartilage is deformed to smooth the adjacent cartilage surfaces (Lin & Klein, 2021). In addition, the continuity of the macroscale pressure, normal fluid flux and Cauchy stress across the interface are explicitly demonstrated from the microscale theory generating further interfacial conditions. The final interfacial condition arises from no normal velocity between the two layers. The constraints provide sufficient conditions to treat the macroscale poroviscoelastic layers as a closed macroscale model, without further need to consider the microscale system at least once constitutive relations are specified. A viscous Newtonian interstitial fluid is assumed in this study, leaving a fixed charge density to be specified, together with the stress-strain relation for the solid scaffold, such as that of Eq. (6.3), while the separation d_f^* is typically unknown so that the shear rate on right hand side of interface condition Eq. (5.38), $-\mu_f^* V^*/d_f^*$, will often have to be treated as constitutive.

As explicitly demonstrated in the simple numerical simulations presented in Section 6, the resulting equations can be solved for two opposing layers of poroviscoelastic media shearing relative to each other, illustrating the macroscale homogenized poroviscoelastic model, including its associated boundary conditions, for the motion of articular cartilage within a skeletal joint. This simplification of a complex microscale model to a macroscale average, including the systematic deduction of boundary conditions, is aimed at facilitating the simulation of cartilage on the joint scale in either physiological or experimental systems, including the prospect of computationally expensive parameter estimation studies. Although such details represent future work, the preliminary and exemplar numerical simulations of the macroscale system presented here indicate how we may examine fundamental aspects of shearing cartilage mechanics, as predicted by the poroviscoelastic model, as well as generating plausible results.

In summary, a closed form macroscopic model for translating poroviscoelastic layers with fixed charge, Newtonian interstitial fluid and a finite deformation viscoelastic solid phase has been derived using a homogenization based on a separation of the pore- and macro- scales. The resulting boundary conditions include a generalization of the Beavers–Joseph interfacial condition. Using a very simple simulation the system is then explored to consider the mechanical effects of oscillatory translation on load bearing in the context of two layers of opposing articular cartilage within a joint. In particular immature cartilage is predicted to undergo greater deformation, with a more extensive temporal oscillation in maximal stress with oscillating load. More generally, this study not only uses simple numerical simulations to highlight complexities of cartilage mechanics even before features such as its anisotropy and depth structure are considered, but also continues the derivation of a macroscale cartilage model, systemically from pore-level foundations predominantly using a homogenization based on a multiple-scale asymptotic analysis.

REFERENCES

- ATESHIAN, G. A. (1997) A theoretical formulation for boundary friction in articular cartilage. *J. Biomech. Eng.*, **119**, 81–86.
- ATESHIAN, G. A. (2009) The role of interstitial fluid pressurization in articular cartilage lubrication. *J. Biomech.*, **42**, 1163–1176.
- ATESHIAN, G. A., LAI, W. M., ZHU, W. B. & MOW, V. C. (1994) An asymptotic solution for the contact of two biphasic cartilage layers. *J. Biomech.*, **27**, 1347–1360.
- ATESHIAN, G. A., WARDEN, W. H., KIM, J. J., GRELSAMER, R. P. & MOW, V. C. (1997) Finite deformation biphasic material properties of bovine articular cartilage from confined compression experiments. *J. Biomech.*, **30**, 1157–1164.
- ATESHIAN, G. A., WANG, H. Q. & LAI, W. M. (1998) The role of interstitial fluid pressurization and surface porosities on the boundary friction of articular cartilage. *J. Tribol.*, **120**, 241–248.
- ATESHIAN, G. A., MAAS, S. & WEISS, J. A. (2013) Multiphasic finite element framework for modeling hydrated mixtures with multiple neutral and charged solutes. *J. Biomech. Eng.*, **135**, 111001.
- AURIAULT, J.-L. (2010) About the Beavers and Joseph boundary condition. *Transport Porous Med.*, **83**, 257–266.
- BEAVERS, G. S. & JOSEPH, D. D. (1967) Boundary conditions at a naturally permeable wall. *J. Fluid Mech.*, **30**, 197–207.
- BROWN, T. D. & SHAW, D. T. (1984) In vitro contact stress distribution on the femoral condyles. *J. Orthop. Res.*, **2**, 190–199.
- BURRIDGE, R. & KELLER, J. B. (1981) Poroelasticity equations derived from microstructure. *J. Acoust. Soc. Am.*, **70**, 1140–1146.
- BUSCHMANN, M. D. & GRODZINSKY, A. J. (1995) A molecular model of proteoglycan–associated electrostatic forces in cartilage mechanics. *J. Biomech. Eng.*, **117**, 179–192.
- CARRARO, T., GOLL, C., MARCINIAK-CZUCHRA, A. & MIKELIĆ, A. (2013) Pressure jump interface law for the Stokes–Darcy coupling: confirmation by direct numerical simulations. *J. Fluid Mech.*, **732**, 510–536.
- CHEN, M. J., KIMPTON, L. S., WHITELEY, J. P., CASTILHO, M., MALDA, J., PLEASE, C. P., WATERS, S. L. & BYRNE, H. M. (2020) Multiscale modelling and homogenisation of fibre-reinforced hydrogels for tissue engineering. *Eur. J. Appl. Math.*, **31**, 143–171.
- COLLIS, J., BROWN, D. L., HUBBARD, M. E. & O'DEA, R. D. (2017) Effective equations governing an active poroelastic medium. *Proc. R Soc. A*, **473**, 20160755.
- DISILVESTRO, M. R. & FRANCIS SUH, J.-K. (2001) A cross-validation of the biphasic poroviscoelastic model of articular cartilage in unconfined compression, indentation, and confined compression. *J. Biomech.*, **34**, 519–525.
- FORSTER, H. & FISHER, J. (1999) The influence of continuous sliding and subsequent surface wear on the friction of articular cartilage. *Proc. Inst. Mech. Eng. H J. Eng. Med.*, **213**, 329–345.

- GALDI, G. P. (2011) *An Introduction to the Mathematical Theory of the Navier–Stokes Equations*. New York: Springer.
- GIRAULT, V. & SEQUEIRA, A. (1991) A well-posed problem for the exterior Stokes equations in two and three dimensions. *Arch. Rational Mech. Anal.*, **114**, 313–333.
- GLEGHORN, J. P. & BONASSAR, L. J. (2008) Lubrication mode analysis of articular cartilage using Stribeck surfaces. *J. Biomech.*, **41**.
- GURTIN, M. E., FRIED, E. & ANAND, L. (2010) *The Mechanics and Thermodynamics of Continua*. Cambridge University Press.
- HARRIGAN, T. P. & MANN, R. W. (1987) State variables for modelling physical aspects of articular cartilage. *Int. J. Solids Struct.*, **23**, 1205–1218.
- HODGE, W. A., FIJAN, R. S., CARLSON, K. L., BURGESS, R. G., HARRIS, W. H. & MANN, R. W. (1986) Contact pressures in the human hip joint measured in vivo. *Proc. Nat. Acad. Sci. U.S.A.*, **83**, 2879–2883.
- HOLMES, M. H. (2013) *Introduction to Perturbation Methods*. New York, USA: Springer.
- HOU, J. S., HOLMES, M. H., LAI, W. M. & MOW, V. C. (1989) Boundary conditions at the cartilage-synovial fluid interface for joint lubrication and theoretical verifications. *Journal of Biomechanical Engineering*, **111**, 78–87.
- HUANG, C. Y., SOLTZ, M. A., KOPACZ, M., MOW, V. C. & ATESHIAN, G. A. Experimental verification of the roles of intrinsic matrix viscoelasticity and tension-compression nonlinearity in the biphasic response of cartilage. *Journal of Biomechanical Engineering-Transactions of the ASME*, **125**(1): 84–93, 2003.
- HUYGHE, J. M. & JANSSEN, J. D. (1997) Quadriphasic mechanics of swelling incompressible porous media. *International Journal of Engineering Science*, **35**, 793–802.
- HUYGHE, J. M., WILSON, W. & MALAKPOOR, K. (2009) On the thermodynamical admissibility of the triphasic theory of charged hydrated tissues. *J. Biomech. Eng.*, **131**, 044504.
- KATTA, J., JIN, Z., INGHAM, E. & FISHER, J. (2008) Biotribology of articular cartilage—a review of the recent advances. *Med. Eng. Phys.*, **30**, 1349–1363.
- KLIKA, V., GAFFNEY, E. A., CHEN, Y.-C. & BROWN, C. P. (2016) An overview of multiphase cartilage mechanical modelling and its role in understanding function and pathology. *J. Mech. Behav. Biomed. Mat.*, **62**, 139–157.
- KLIKA, V., WHITELEY, J. P., BROWN, C. P. & GAFFNEY, E. A. (2019) The combined impact of tissue heterogeneity and fixed charge for models of cartilage: the one-dimensional biphasic swelling model revisited. *Biomech. Model. Mechanobiol.*, **18**, 953–968.
- KNOX, P., LEVICK, J. R. & McDONALD, J. N. (1988) Synovial fluid—its mass, macromolecular content and pressure in major limb joints of the rabbit. *Q. J. Exp. Physiol.*, **73**, 33–45.
- LACIS, U. & BAGHERI, S. (2017) A framework for computing effective boundary conditions at the interface between free fluid and a porous medium. *J. Fluid Mech.*, **812**, 866–889.
- LIAO, J., SMITH, D. W., MIRAMINI, S., THIBBOTUWAWA, N., GARDINER, B. S. & ZHANG, L. (2019) The investigation of fluid flow in cartilage contact gap. *J. Mech. Behav. Biomed. Mat.*, **95**, 153–164.
- LIAO, J., MIRAMINI, S., LIU, X. & ZHANG, L. (2020) Computational study on synovial fluid flow behaviour in cartilage contact gap under osteoarthritic condition. *Comput. Biol. Med.*, **123**, 103915.
- LIN, W. & KLEIN, J. (2021) Recent progress in cartilage lubrication. *Adv. Mat.*, **33**, 2005513.
- LU, X. L., WAN, L. Q., GUO, X. E. & MOW, V. C. (2010) A linearized formulation of triphasic mixture theory for articular cartilage, and its application to indentation analysis. *J. Biomech.*, **43**, 673–679.
- LUCA, E. & CROWDY, D. G. (2018) A transform method for the biharmonic equation in multiply connected circular domains. *IMA J. Appl. Math.*, **83**, 942–976.
- LUNN, M. (1991) *A First Course in Mechanics*. Oxford, UK: Oxford University Press.
- MARCINIAK-CZOCHRA, A. & MIKELIĆ, A. (2012) Effective pressure interface law for transport phenomena between an unconfined fluid and a porous medium using homogenization. *Multiscale Model. Simul.*, **10**, 285–305.
- MAROUDAS, A., BULLOUGH, P., SWANSON, S. A. V. & FREEMAN, M. A. R. (1968) The permeability of articular cartilage. *J. Bone Joint Surg.*, **50B**, 166–177.
- MIKELIC, A. & JÄGER, W. (2000) On the interface boundary condition of Beavers, Joseph, and Saffman. *SIAM J. Appl. Math.*, **60**, 1111–1127.

- MOW, V. C., HOLMES, M. H. & LAI, W. M. (1980a) Fluid transport and mechanical properties of articular cartilage: A review., *Journal of Biomechanics*, **17**, 377–394.
- MOW, V. C., KUEI, S. C., LAI, W. M. & ARMSTRONG, C. G. (1980b) Biphasic creep and stress relaxation of articular cartilage in compression: theory and experiments. *J. Biomech. Eng.*, **102**, 73–84.
- MOW, V. C., KWAN, M. K., LAI, W. M. & HOLMES, M. H. (1986) A finite deformation theory for nonlinearly permeable soft hydrated biological tissues. *Frontiers in Biomechanics*. Springer, pp. 153–179.
- MOW, V. C., GIBBS, M. C., LAI, W. M., ZHU, W. B. & ATHANASIOU, K. A. (1989) Biphasic indentation of articular cartilage. 2. A numerical algorithm and an experimental study. *J. Biomech.*, **22**, 853–861.
- MOW, V. C., RATCLIFFE, A. & ROBIN POOLE, A. (1992) Cartilage and diarthrodial joints as paradigms for hierarchical materials and structures. *Biomaterials*, **13**, 67–97.
- MOW, V. C., ATESHIAN, G. A. & SPILKER, R. L. (1993) Biomechanics of diarthrodial joints: a review of twenty years of progress. *J. Biomech. Eng.*, **115**, 460–467.
- MURAD, M. A. & LOULA, A. F. (1994) On stability and convergence of finite element approximations of Biot's consolidation problem. *Int. J. Numer. Meth. Engng.*, **37**, 645–667.
- NAGEL, T. & KELLY, D. J. (2010) The influence of fiber orientation on the equilibrium properties of neutral and charged biphasic tissues. *J. Biomech. Eng.*, **132**, 114506.
- NORDSLETTEN, D., KAY, D. & SMITH, N. (2010) A non-conforming monolithic finite element method for problems of coupled mechanics. *J. Comput. Phys.*, **229**, 7571–7593.
- PENTA, R. & GERISCH, A. (2018) An introduction to asymptotic homogenization. *Multiscale Models in Mechano and Tumor Biology* (A. GERISCH, R. PENTA & J. LANG eds). Springer, pp. 1–26.
- PENTA, R., AMBROSI, D. & SHIPLEY, R. J. (2014) Effective governing equations for poroelastic growing media. *Q. J. Mech. Appl. Math.*, **67**, 69–91.
- PENTA, R., MILLER, L., GRILLO, A., RAMÍREZ-TORRES, A., MASCHERONI, P. & RODRÍGUEZ-RAMOS, R. (2019) Porosity and diffusion in biological tissues. recent advances and further perspectives. *Constitutive Modelling of Solid Continua* (J. MERODIO & R. OGDEN eds), vol. **262**. Cham: Springer, pp. 311–356.
- POZRIKIDIS, C. (1992) *Boundary Integral and Singularity Methods for Linearized Viscous Flow*. Cambridge, UK: Cambridge University Press.
- RAMÍREZ-TORRES, A., DI STEFANO, S., GRILLO, A., RODRÍGUEZ-RAMOS, R., MERODIO, J. & PENTA, R. (2018) An asymptotic homogenization approach to the microstructural evolution of heterogeneous media. *Int. J. Non-Lin. Mech.*, **106**, 245–257.
- ROHAN, E., NAILI, S. & NGUYEN, V.-H. (2016) Wave propagation in a strongly heterogeneous elastic porous medium: homogenization of biot medium with double porosities. *Comp. Rend. Mec.*, **344**, 569–581.
- SAFFMAN, P. G. (1971) On the boundary condition at the surface of a porous medium. *Stud. Appl. Math.*, **1**, 93–101.
- SHEPHERD, D. E. T. & SEEDHOM, B. B. (1999) The 'instantaneous' compressive modulus of human articular cartilage in joints of the lower limb. *Rheumatology*, **38**, 124–132.
- SMYTH, P. A., RIFKIN, R. E., JACKSON, R. L. & HANSON, R. R. (2012) A surface roughness comparison of cartilage in different types of synovial joints. *J. Biomech. Eng.*, **134**, 021006.
- WHITELEY, J. P. & GAFFNEY, E. A. (2020) Modelling the inclusion of swelling pressure in a tissue level poroviscoelastic model of cartilage deformation. *Math. Med. Biol.*, **37**, 390–429.
- WILSON, W., VAN DONKELAAR, C. C., VAN RIETBERGEN, B. & HUISKES, R. (2005) A fibril-reinforced poroviscoelastic swelling model for articular cartilage. *Journal of Biomechanics*, **38**, 1195–1204.
- WU, Y. & FERGUSON, S. J. (2017) The influence of cartilage surface topography on fluid flow in the intra-articular gap. *Comput. Methods Biomech. Biomed. Eng.*, **20**, 250–259.
- WU, J. Z., HERZOG, W. & EPSTEIN, M. (1998) Evaluation of the finite element software ABAQUS for biomechanical modelling of biphasic tissues. *J. Biomech.*, **31**, 165–169.

A. Investigating the transition and fluid layers

In this appendix we first provide general analytical support to the numerical observation presented in Section 5.2 that there is no pressure drop across the fluid and transition layers in the microscale cell, illustrated in Fig. 2, which we have homogenized over. We then demonstrate that oscillatory velocity components are suppressed in the centre of the fluid region. As a consequence, at leading order, the average flow in the centre of the fluid region is a simple shear flow, resulting in a deviatoric Cauchy stress tensor containing only constant off-diagonal entries. This provides further evidence to back up the conclusions from the numerical results presented in Section 5.2, as well as additionally supporting the use of Eqs. (5.27), (5.28) in deducing the generalization of the Beavers–Joseph interfacial condition.

Throughout this appendix we assume that, at a fixed point in time, the geometry of the upper transition layer shown in Fig. 2 has a reflection symmetry in a plane $y_1 = a$. Similarly we assume that, at the same point in time, the lower transition layer has a reflection symmetry in a plane $y_1 = b$. In Fig. 2, seen as a snapshot in time, such a plane of symmetry for the lower transition region is given by either dashed line. Such a plane exists for the upper transition layer, though it is offset by a translation in y_1 from the dashed lines and thus the figure depicts the case where $a \neq b$. We provide analytical evidence for a zero drop in pressure across the interface for the case $a = b$ in two dimensions in Section A.1, before considering the more general case $a \neq b$ in two dimensions in Section A.2, allowing us to justify why the leading order velocity may be approximated by a simple shearing flow in Section A.3. We then give a demonstration that these results generalize to three dimensions in Section A.4.

A.1 Justification of no pressure drop for symmetric transition layers with $a = b$ in 2D

We first assume that the scaffold geometry in both the upper and lower transition layers has a symmetry with respect to a reflection in a plane of constant $y_1 = a = b$. This is restrictive as the upper and lower transitions are in relative motion; for unit velocity and spatial dimensions if it holds at time t_1 then it will hold at times $t_1 + n$, $n \in \mathbb{Z}$. As this is a simpler case, we consider it first.

To proceed, without loss of generality, we set $a = b = 0$, so that the geometry has a reflection symmetry in $y_1 = 0$ and, noting unit periodicity in the y_1 direction, we thus have periodic boundary conditions at $y_1 = \pm 1/2$. Then we consider the parity symmetry of the microscale cell problem of Section 5.2, Eqs. (5.9)–(5.13) with $\mathbf{V}^{-1} = (1 \ 0 \ 0)^\top$, so that $(1 \ 0 \ 0)^\top$ is imposed as the boundary velocity for all inhomogeneous Dirichlet boundary conditions and limits. We first deduce a reflection parity symmetry.

Proposition 1. *If the geometry is invariant under the reflection $y_1 \rightarrow -y_1$ then solution of the microscale cell problem of Section 5.2, Eqs. (5.9)–(5.13) with $\mathbf{V}^{-1} = (1 \ 0 \ 0)^\top$, is such that the pressure is of odd parity.*

Proof. Let (v_1, v_3, p) be the solution of this microscale problem and let

$$s_1(y_1, y_3) = -v_1(-y_1, y_3), \quad s_3(y_1, y_3) = v_3(-y_1, y_3), \quad r(y_1, y_3) = p(-y_1, y_3). \quad (\text{A.1})$$

Then noting the geometry is invariant under reflection $y_1 \rightarrow -y_1$ we have (s_1, s_3, r) solves the microscale cell problem with $(-1 \ 0 \ 0)^\top$ imposed as the boundary velocity for all inhomogeneous Dirichlet boundary conditions and limits. Hence, by linearity, $(s_1 + v_1, s_3 + v_3, r + p)$ solve the microscale cell problem with all velocity conditions zero, as does the trivial solution by inspection.

That the only solution is the trivial solution with zero velocity and constant pressure arises from a uniqueness argument, which follows from the identity (Pozrikidis, 1992):

$$\int_{\partial V} v_i \sigma_{ij} n_j dS = -2 \int_V \left(\frac{\partial v_j}{\partial x_i} + \frac{\partial v_i}{\partial x_j} \right) \left(\frac{\partial v_j}{\partial x_i} + \frac{\partial v_i}{\partial x_j} \right) dV,$$

where V is the region of fluid in the microscale cell and ∂V its boundary. The left hand integral is zero as (i) the contribution on a face of the microscale cell's boundary where periodicity is imposed is cancelled by the contribution on the opposite boundary due to the sign change in the outward normal \mathbf{n} ; and (ii) zero velocities are imposed for the remaining velocity boundary conditions. The integrand on the right hand side is, to within a multiplicative constant, the rate of viscous working which thus is zero. The only possible flow in the absence of viscous working is that of rigid body motion with constant pressure (Pozrikidis, 1992), but the zero boundary conditions force the velocity and angular velocity of the rigid body flow to be zero while, without loss of generality, the constant pressure can be set to zero. Thus $(s_1 + v_1, s_3 + v_3, r + p)$ is zero and hence

$$v_1(y_1, y_3) = v_1(-y_1, y_3), \quad v_3(y_1, y_3) = -v_3(-y_1, y_3), \quad p(y_1, y_3) = -p(-y_1, y_3),$$

giving that v_1 has even parity and v_3, p have odd parity under the reflection. \square

To proceed, let the range of y_3 in the microscale cell problem be denoted by $[y_3^{\min}, y_3^{\max}]$, which was infinite in the analytical problem of Eqs. (5.9)–(5.13), though of course finite in the numerical investigations of Section 5.2. Since p is odd, we have

$$\int_{-1/2}^{1/2} p(y_1, y_3^{\max}) dy_1 = \int_{-1/2}^{1/2} p(y_1, y_3^{\min}) dy_1 = 0, \quad (\text{A.2})$$

and periodicity implies this result is invariant under any translation in y_1 . Hence there is no jump in the average pressure across the transition and fluid layers, which is sufficient for there to be no jump in the macroscale pressure to be matched across the transition and fluid layers.

A.2 Justification of no pressure drop for symmetric transition layers with $a \neq b$ in 2D

We now extend our justification of zero pressure drop across the interface to the case where $a \neq b$. We first demonstrate that the y_1 dependence of both vorticity and velocity is suppressed in the centre of the fluid layer in Sections A.2.1 and A.2.2, before deriving a symmetry condition to justify the zero pressure drop in Section A.2.3.

A.2.1 The y_1 dependence of vorticity in the fluid layer. We define the only non-zero component of vorticity to be the scalar ω given by

$$\omega = \frac{\partial v_3}{\partial y_1} - \frac{\partial v_1}{\partial y_3}, \quad (\text{A.3})$$

which represents the y_2 component of the vorticity. In particular ω can be evaluated at $y_3 = y_3^-, y_3^+$ corresponding to the dotted lines of Fig. 2, which separate the fluid layer from the transition layers. These vorticities can be written as Fourier series:

$$\omega(y_1, y_3^\pm) = \frac{1}{2} a_0^\pm + \sum_m (a_m^\pm \cos(2\pi m y_1) + b_m^\pm \sin(2\pi m y_1)),$$

where we have also used the observation of Section 5.2 that there is no y_2 dependence to the cell problem.

By taking the curl of the momentum equation one may deduced that ω is harmonic. Hence in the fluid layer we have

$$\nabla^2 \omega = 0, \quad y_1 \in [-1/2, 1/2], \quad y_3 \in [y_3^-, y_3^+],$$

with periodicity at $y_1 = \pm 1/2$. We therefore seek a solution for ω that is the Fourier expansion

$$\omega(y_1, y_3) = \frac{1}{2} a_0(y_3) + \sum_{m \neq 0} (a_m(y_3) \cos(2\pi m y_1) + b_m(y_3) \sin(2\pi m y_1)), \quad (\text{A.4})$$

allowing one to determine features of ω and thus the velocity field.

We now show that the non-constant modes decay exponentially fast on moving into the interior of the fluid layer. Noting linearity we focus on the $\cos(2\pi y_1)$ mode, where the fact ω is harmonic entails

$$a_1'' - 4\pi^2 a_1 = 0, \quad a_1(y_3^-) = a_1^-, \quad a_1(y_3^+) = a_1^+,$$

with the prime denoting differentiation with respect to y_3 . To solve for a_1 it is simpler to consider the scaled coordinate

$$q_3 = \frac{y_3 - y_3^-}{y_3^+ - y_3^-} = \frac{y_3 - y_3^-}{d_f^0},$$

where d_f^0 is the leading order fluid region thickness, which is constant at the level of approximation in this paper, as detailed in Section 5.1. Note that, without loss of generality, the origin of the y_3 axis is taken to coincide with the midpoint of the fluid layer, which corresponds to $q_3 = 1/2$. We then have

$$\begin{aligned} a_1(y_3) &= \frac{a_1^- - a_1^+ e^{-2\pi d_f^0}}{1 - e^{-4\pi d_f^0}} e^{-2\pi d_f^0 q_3} + \frac{a_1^+ - a_1^- e^{-2\pi d_f^0}}{1 - e^{-4\pi d_f^0}} e^{-2\pi d_f^0 (1-q_3)} \\ &\approx a_1^- e^{-2\pi d_f^0 q_3} + a_1^+ e^{-2\pi d_f^0 (1-q_3)}, \end{aligned} \quad (\text{A.5})$$

where for the parameters used in the simulations presented in Fig. 3, $d_f^0 = 2$ and $\exp(-2\pi d_f^0) \sim 3 \times 10^{-6}$, justifying the above approximation. In the middle of the fluid region, where $q_3 \approx 1/2$, we see the vorticity for this mode is suppressed by a factor of $\exp(-\pi d_f^0) = \exp(-2\pi) \sim 2 \times 10^{-3}$, and it is clear higher order modes will be suppressed even more extensively. In summary the y_1 oscillations are suppressed by a factor of at least $\exp(-2\pi)$ in the centre of the fluid region provided the thickness of the fluid region is not small relative to the pore lengthscale. We assume that this is not the case, as a fluid layer between the two poroviscoelastic bodies that is significantly thinner than the pore size would require modelling at the sub-nanometre scale. This is an unphysiological regime; for instance such lengthscales are far less than measured cartilage surface roughness (Smyth *et al.*, 2012). Furthermore, the continuum approximation would be likely to break down under these circumstances.

A.2.2 The y_1 dependence of velocity in the fluid layer. We now consider the flow fields. Using incompressibility of the fluid and the definition of vorticity given by Eq. (A.3) we have

$$\begin{aligned}\frac{\partial v_1}{\partial y_1} + \frac{\partial v_3}{\partial y_3} &= 0, \\ \frac{\partial v_3}{\partial y_1} - \frac{\partial v_1}{\partial y_3} &= \frac{1}{2}a_0(y_3) + \sum_m (a_m(y_3) \cos(2\pi m y_1) + b_m(y_3) \sin(2\pi m y_1)).\end{aligned}$$

With the first harmonic mode

$$v_1 = j_1(y_3) \cos(2\pi y_1) + k_1(y_3) \sin(2\pi y_1), \quad v_3 = m_1(y_3) \cos(2\pi y_1) + n_1(y_3) \sin(2\pi y_1),$$

we have, from the first sine harmonic of the continuity equation and the first cosine harmonic of the vorticity equation, that

$$-2\pi j_1 + n_1' = 0, \quad 2\pi n_1 - j_1' = a_1(y_3),$$

where $a_1(y_3)$ is given by Eq. (A.5). Rewriting in terms of q_3 with the prime now denoting the derivative with respect to q_3 we have

$$n_1'' - 4\pi^2 (d_f^0)^2 n_1 = a_1(y_3(q_3)) \approx a_1^- e^{-2\pi d_f^0 q_3} + a_1^+ e^{-2\pi d_f^0 (1-q_3)}.$$

The complementary functions will decay in the same manner as those of the vorticity since the homogeneous equation is the same. Treating the approximate expression for $a_1(y_3)$ as exact, the particular integral is

$$-\frac{a_1^-}{4\pi d_f^0} q_3 e^{-2\pi d_f^0 q_3} + \frac{a_1^+}{4\pi d_f^0} q_3 e^{-2\pi d_f^0 (1-q_3)},$$

which is also suppressed for the middle of the fluid region where $q_3 \approx 1/2$. Similar results hold for all the other Fourier coefficients and hence the y_1 -oscillatory harmonics of the velocity are also suppressed.

A.2.3 Justification that the half-cell problem is approximately reflection invariant. We have that the y_1 -dependent velocity terms in the centre of the fluid layer are suppressed compared to those at the interface of the transition and fluid regions, i.e. the dotted lines in Fig. 2, by a factor of $\exp(-\pi d_f^0)$ for the first harmonic mode and, analogously, one can show the suppression factor is $\exp(-m\pi d_f^0)$ for the m^{th} mode.

We can thus consider the lower half of the cell in Fig. 2, with the upper half proceeding analogously. Firstly, as the lower layer is moving we shift the y_1 coordinate so that at any fixed point in time $y_1 = 0$ is a plane of reflection symmetry of the lower layer geometry. The time dependence of this shift has no effect on the governing fluid equations as there are no time derivatives in Stokes flow. Thus we have the domain

$$\left\{ (y_1, y_3) \mid y_1 \in (-1/2, 1/2), y_3 \in (y_3^{\min}, 0) \right\},$$

with a reflection symmetry of the geometry at $y_1 = 0$, with the velocity and pressure satisfying Eqs. (5.9)–(5.13), except that the velocity condition as $y_3 \rightarrow \infty$ is replaced by a velocity condition on $y_3 = 0$. From the above sections we have that this velocity condition has no y_1 dependence to excellent approximation, and we drop the y_1 dependence.

Noting that Stokes equations are linear, the difference between the full and approximate problems satisfies the same bulk equations. The difference in the solutions is given by the solution for Stokes flow in the half-cell with homogeneous boundary conditions, save the small difference in velocity at $y_3 = 0$. Furthermore the Stokes problem is well posed, as can be inferred for the weak Stokes problem from the results of Girault & Sequeira (1991) with $y_3 \in [y_3^{\min}, y_3^{\max}]$ to ensure the L_2 norm exists. Hence we have that the small errors on the boundary at $y_3 = 0$ are not anticipated to induce significant error in the solution.

With y_1 independent boundary conditions, we have that the geometry and boundary conditions are invariant under $y_1 \rightarrow -y_1$ and the pressure is odd, analogously to Proposition 1 of Section A.1. Hence

$$\int_{-1/2}^{1/2} p(y_1, 0) dy_1 = \int_{-1/2}^{1/2} p(y_1, y_3^{\min}) dy_1 = 0. \quad (\text{A.6})$$

Treating the upper layer in the same manner, and taking into account the plane of symmetry is now at $y_1 = a - b$, we have from the fact p is odd with respect to reflection in $y_1 = a - b$:

$$\int_{a-b-1/2}^{a-b+1/2} p(y_1, 0) dy_1 = \int_{a-b-1/2}^{a-b+1/2} p(y_1, y_3^{\max}) dy_1 = 0. \quad (\text{A.7})$$

In principle the upper and lower problems could have different pressure gauges, whereby the pressure in the upper problem is shifted by a constant relative to the pressure in the lower problem. However, the requirement that these are the upper and lower half of the full microscale cell problem entails the constant pressure shift must be zero. This is indeed the case else the pressure averages on $y_3 = 0$ would differ, and so

$$\int_{a-b-1/2}^{a-b+1/2} p(y_1, 0) dy_1 = \int_{-1/2}^{1/2} p(y_1, 0) dy_1 = 0 \quad (\text{A.8})$$

by periodicity. Hence by considering Eqs. (A.6)–(A.8) we predict that there is no jump in the pressure averaged over y_1 on traversing the upper transition, fluid and lower transition layers; this is sufficient for there to be no jump in the macroscale pressure to be matched across the transition and fluid layers.

Note that the full cell problem has a potential time dependence as the relative displacement of the upper and lower scaffolds changes with time as the lower scaffold translates. However, there is no time dependence in the upper half-cell problem nor the lower half-cell problem towards the centre of the fluid layer to excellent approximation as the upper and lower halves are decoupled and independent of y_1 , the translating coordinate of the lower cell. Hence, the full cell problem has no time dependence to excellent approximation.

A.3 Justification of shear flow in the fluid layer in 2D

First note that the off-diagonal fluid region Cauchy stress averages of Eq. (5.24) at leading order simplify, e.g.

$$\Sigma_{13}^f = \int \left(\frac{\partial v_3}{\partial y_1} + \frac{\partial v_1}{\partial y_3} \right) dy_1 dy_2 = \int_{-1/2}^{1/2} \frac{\partial v_1}{\partial y_3} dy_1 = \frac{d}{dy_3} \int_{-1/2}^{1/2} v_1 dy_1 = \frac{d\tilde{v}_1}{dy_3}, \quad (\text{A.9})$$

where the y_2 independence allows a trivial integration, periodicity in y_1 removes one of the integrands and \tilde{v}_1 is the zeroth mode for v_1 in the fluid region.

We first of all consider the upper half of the microscale cell, with $y_3 \geq 0$. The pressure p is odd with respect to reflection in $y_1 = a - b$, at the leading order of the level of accuracy of the previous section.

Hence, at leading order, its zero pressure mode in the fluid region, $p_0(y_3)$, is zero by parity as it must be zero at $y_1 = a - b$ and the zeroth harmonic mode has no y_1 dependence. Taking the zeroth harmonic mode of the momentum equation, one immediately finds that the zeroth mode for v_1 in the fluid region, denoted \tilde{v}_1 , satisfies

$$(\tilde{v}_1)'' = 0, \quad \tilde{v}_1 = \alpha y_3 + \beta = \Sigma_{13}^f y_3 + \beta, \quad (\text{A10})$$

where $\alpha = \Sigma_{13}^f$, β are independent of y_1 and y_3 . Furthermore the flow towards the centre of the fluid region is time independent to excellent approximation and thus α , β are constant. Similar remarks apply for the lower half of the microscale cell, and continuity of pore-scale velocity and stress at $y_3 = 0$ demands the constants α , β are the same in each half. Hence at leading order the average off-diagonal fluid region Cauchy stress average, Σ_{31}^f , is constant, which is consistent with Eq. (5.24).

Working with the leading order velocity, extending the definition of \tilde{v}_3^0 in Eq. (5.31) into the fluid layer, so that

$$\tilde{v}_3^0 = \int v_3^0 dy_1 dy_2, \quad y_3 \in [y_3^-, y_3^+], \quad (\text{A.11})$$

we also have

$$\frac{d\tilde{v}_3^0}{dy_3} = \int \frac{\partial v_3^0}{\partial y_3} dy_1 dy_2 = 0,$$

with the final equality arising from incompressibility and periodicity. Combining this with Eq. (5.33) gives

$$\tilde{v}_3^0(y_3^{\min}) = \tilde{v}_3^0(y_3^{\max}) = \tilde{v}_3^0(y_3), \quad y_3 \in [y_3^-, y_3^+]$$

while the zero velocity boundary conditions at y_3^{\min} , y_3^{\max} entail all these terms are zero.

Hence the average flow in the fluid region is a simple shear flow at leading order. Furthermore, towards the centre of the fluid region, the non-zero harmonic terms are suppressed and thus the flow fields are the same as their averages to leading order and we have a simple shear flow at leading order in the central fluid region, as observed in Fig. 3. From Eq. (A.10) we also have

$$\Sigma_{31}^f = \frac{\tilde{v}_1(y_3^+) - \tilde{v}_1(y_3^-)}{y_3^+ - y_3^-} = \frac{\tilde{v}_1(y_3^+) - \tilde{v}_1(y_3^-)}{d_f^0}.$$

Noting from numerical simulations, e.g. Fig. 3, which v_1 approaches the speed of the scaffold in the transition layer on passing into this region in the fluid layer we have

$$\Sigma_{31}^f = -\frac{V_1^{-1}}{d_f^0}$$

from the condition of Eq. (5.11), where the value here of $V_1^{-1} = 1$ generalizes immediately by linearity, providing further justification for Eq. (5.27). More generally assuming without loss $y_3 = 0$ is the centre of the fluid layer, so that $y_3^+ = -y_3^-$, and that v_1 approaches the speed of the scaffold in the transition layer on passing into this region, with the upper transition fixed and the lower region moving at speed

$\mathbf{V}^{-1} = (1 \ 0 \ 0)^\top$, we have

$$\tilde{v}_1 = \frac{y_3}{d_f^0} + \frac{1}{2},$$

which is consistent with Fig. 3. If the upper and lower scaffolds are the same except for the translation in y_1 with the lower scaffold movement then, when the scaffolds align at integer intervals in time, there is a discrete symmetry $(v_1, v_3, p) \rightarrow (1 - v_1, v_3, p)$ when $y_3 \rightarrow -y_3$. By the techniques of Section A.1 one can then show that $v_1 = 1 - v_1$ when $y_3 = -y_3$ and thus $v_1(y_1, y_2, 0) = 1/2$, which shows $\beta = 1/2$ at the integer intervals in time coinciding with scaffold alignment. The time independence of β then gives $\beta = 1/2$ for all time independently confirming $\beta = 1/2$ in the special case that the scaffolds are the same in the upper and lower transition layers.

We finally note that this analysis requires the film thickness is on the pore scale or larger, so that $d_f^0 = \mathcal{O}(1)$ or larger, which is reasonable physiologically given the nanoscale pore size. Furthermore a layer significantly thinner than the pore size would be considering a sub-nanometre scale where the continuum approximation would break down and thus we do not consider this case.

A.4 Three spatial dimensions

The above justification of the properties of the flow, that it is a simple shear with no pressure jump, was determined in the idealization of a 2D system. It generalizes to 3D system, which thus now includes a y_2 direction perpendicular to the y_1 and y_3 directions of Fig. 3. The velocity of the lower scaffold is still $\mathbf{V}^{-1} = (1 \ 0 \ 0)^\top$ below, but we now assume periodicity of the scaffold in the transition region in the y_2 direction, with unit period.

A.4.1 Aligned upper and lower scaffolds: symmetry. If the upper and lower scaffolds are aligned, the symmetry argument of Section A.1 will generalize immediately. In particular if, without loss of generality, the geometry has even parity with respect to the planes $y_1 = 0$, $y_2 = 0$ and (v_1, v_2, v_3, p) is the solution of this microscale problem, then we may generalize Eq. (A.1) by considering

$$\begin{aligned} s_1(y_1, y_2, y_3) &= -v_1(-y_1, y_2, y_3), & s_2(y_1, y_2, y_3) &= -v_2(-y_1, y_2, y_3), \\ s_3(y_1, y_2, y_3) &= v_3(-y_1, y_2, y_3), & r(y_1, y_2, y_3) &= p(-y_1, y_2, y_3), \end{aligned}$$

to deduce that $p(y_1, y_2, y_3) = -p(-y_1, y_2, y_3)$. Similarly, we consider the two sets of functions

$$\begin{aligned} g_1(y_1, y_2, y_3) &= -v_1(y_1, -y_2, y_3), & g_2^\pm(y_1, y_2, y_3) &= \pm v_2(y_1, -y_2, y_3), \\ g_3(y_1, y_2, y_3) &= v_3(y_1, -y_2, y_3), & h(y_1, y_2, y_3) &= p(y_1, -y_2, y_3). \end{aligned}$$

Working with (g_1, g_2^-, g_3, h) gives $v_2(y_1, y_2, y_3) = v_2(y_1, -y_2, y_3)$ and $p(y_1, y_2, y_3) = -p(y_1, -y_2, y_3)$. The latter gives

$$\int_{-1/2}^{1/2} \int_{-1/2}^{1/2} p(y_1, y_3^{max}) dy_1 dy_2 = \int_{-1/2}^{1/2} \int_{-1/2}^{1/2} p(y_1, y_3^{min}) dy_1 dy_2 = 0, \quad (\text{A.12})$$

which is sufficient for no jump in the macroscale pressure across the transition and fluid layers. Furthermore working instead with (g_1, g_2^+, g_3, h) gives $v_2(y_1, y_2, y_3) = -v_2(y_1, -y_2, y_3)$ and hence v_2 is both even and odd under a y_2 reflection, and thus identically zero, when the scaffolds are aligned.

A.4.2 *Unaligned upper and lower scaffolds.* For the fluid layer, with $y_3 \in [y_3^-, y_3^+]$, we have the vorticity $\boldsymbol{\omega} = \nabla \wedge \mathbf{v}$ satisfies

$$\nabla \cdot \boldsymbol{\omega} = 0, \quad \nabla^2 \boldsymbol{\omega} = \mathbf{0}, \quad (\text{A.13})$$

where the final equality arises from the curl of the momentum equation. Overloading the symbol \mathbf{n} to here denote $\mathbf{n} = (n_1, n_2)$, with n_1, n_2 integer, we use the periodicity in y_1, y_2 to generalize the Fourier expansion of Eq. (A.4) to

$$\boldsymbol{\omega} = \frac{1}{4} \mathbf{a}_0(y_3) + \sum_{\mathbf{n} \neq (0,0)} \text{Re} \left(e^{2\pi i \mathbf{n} \cdot (y_1, y_2)} \mathbf{a}_{\mathbf{n}}(y_3) \right), \quad (\text{A.14})$$

where $\mathbf{a}_{\mathbf{n}} = (a_{1\mathbf{n}}, a_{2\mathbf{n}}, a_{3\mathbf{n}})$ are the y_3 and possibly time dependent Fourier coefficients. From Eqs. (A.13) and (A.14) we have

$$\frac{da_{3\mathbf{n}}}{dy_3} + 2\pi i (n_1 a_{1\mathbf{n}} + n_2 a_{2\mathbf{n}}) = 0, \quad \frac{d^2 \mathbf{a}_{\mathbf{n}}}{dy_3^2} - 4\pi^2 |\mathbf{n}|^2 \mathbf{a}_{\mathbf{n}} = 0. \quad (\text{A.15})$$

With boundary conditions $\mathbf{a}_{\mathbf{n}}^\pm$ at $y_3 = y_3^\pm$ and

$$q_3 = \frac{y_3 - y_3^-}{y_3^+ - y_3^-} = \frac{y_3 - y_3^-}{d_f^0},$$

the latter constraint on $\mathbf{a}_{\mathbf{n}}$ gives, for $\mathbf{n} \neq (0, 0)$,

$$\mathbf{a}_{\mathbf{n}} \approx \mathbf{a}_{\mathbf{n}}^- e^{-2\pi d_f^0 q_3} + \mathbf{a}_{\mathbf{n}}^+ e^{-2\pi d_f^0 (1-q_3)},$$

by direct analogy to the 2D case with terms of the order $\exp(-2\pi d_f^0) \sim 3 \times 10^{-6}$ dropped. We note the boundary conditions $\mathbf{a}_{\mathbf{n}}^\pm$ at $y_3 = y_3^\pm$ are not independent and must be such that the first constraint of Eq. (A.15) can be satisfied. This is not true for general boundary conditions but taking the boundary conditions from the vorticity of the exact solution to the Stokes equation (which exists, Ch.V.2, Galdi (2011)) ensures a divergenceless vorticity and the required constraints hold. Thus as previously we have exponential suppression of the vorticity towards the centre of the fluid region.

The velocity field satisfies

$$\nabla \cdot \mathbf{v} = 0, \quad \nabla \wedge \mathbf{v} = \boldsymbol{\omega}, \quad (\text{A.16})$$

and we introduce a vector potential \mathbf{b} such that $\mathbf{v} = \nabla \wedge \mathbf{b}$. Use of the gauge freedom $\mathbf{b} \rightarrow \mathbf{b} + \nabla \psi$ for any potential ψ entails $\nabla \cdot \mathbf{b} = 0$ without loss of generality, whence

$$\nabla \cdot \mathbf{b} = 0, \quad \nabla^2 \mathbf{b} = -\boldsymbol{\omega}. \quad (\text{A.17})$$

With a Fourier expansion

$$\mathbf{b} = \frac{1}{4} \mathbf{b}_0(y_3) + \sum_{\mathbf{n} \neq (0,0)} \text{Re} \left(e^{2\pi i \mathbf{n} \cdot (y_1, y_2)} \mathbf{b}_{\mathbf{n}}(y_3) \right), \quad (\text{A.18})$$

one may solve for the Fourier coefficients $\mathbf{b}_{\mathbf{n}}(y_3)$ for both the homogeneous solution, which is the complementary function, and the particular integral for the inhomogeneous forcing, $-\boldsymbol{\omega}$, noting the Fourier modes are not fully independent but coupled by the divergenceless condition, analogous to the above reasoning. As in the previous sections, and as may be deduced by explicit calculation, the Fourier

modes $\mathbf{b}_{\mathbf{n}}(y_3)$ for $\mathbf{n} \neq (0, 0)$ will be exponentially suppressed towards the centre of the fluid region, a property that will not be altered on taking a curl and thus will also be inherited by the velocity field \mathbf{v} . Hence the y_1, y_2 variation of the velocity field \mathbf{v} will be exponentially suppressed towards the centre of the fluid region.

Thus the approximate reflection invariances of the lower and upper half-cell problems can be deduced by direct analogy to Section A.2.3 with, e.g. Eq. (A.6) for the lower half-cell generalizing to

$$\int_{-1/2}^{1/2} \int_{-1/2}^{1/2} p(y_1, 0) dy_1 dy_2 = \int_{-1/2}^{1/2} \int_{-1/2}^{1/2} p(y_1, y_3^{\min}) dy_1 dy_2 = 0, \quad (\text{A.19})$$

with (approximate) reflection invariance in the planes $y_1 = 0$, $y_2 = 0$ for the lower half-cell. Analogous results hold for the upper half-cell and thus once more there is no jump in the macroscale pressure; also, by direct analogy to the reasoning of Section A.2.3, to excellent approximation there is no time dependence towards the centre of the fluid layer.

A.4.3 Justification of shear flow in the fluid layer. By direct analogy with Section A.2.3 we have, with $i = 1, 2$,

$$\tilde{v}_i = \int_{-1/2}^{1/2} \int_{-1/2}^{1/2} v_i dy_1 dy_2, \quad \Sigma_{i3}^f = \frac{d\tilde{v}_i}{dy_3}, \quad \frac{d^2\tilde{v}_i}{dy_3^2} = 0, \quad \tilde{v}_i = \alpha_i y_3 + \beta_i = \Sigma_{i3}^f y_3 + \beta_i, \quad (\text{A20})$$

with $\alpha_i = \Sigma_{i3}^f$, β_i constant. Noting v_2 is identically zero at the integer time intervals when the upper and lower scaffolds are aligned and that α_2 , β_2 are time independent we have $\tilde{v}_2 = 0$ for all time. Further, the results of Eq. (A.11) *et. seq.* still hold in this more general context and thus $\tilde{v}_3 = 0$ and the averaged velocities in the fluid layer constitute a simple shear flow, which is the flow to leading order as oscillatory terms are suppressed in the fluid layer.

Furthermore, as previously, on making the assumption v_1 approaches the speed of the scaffold in the transition layer on passing into this region in the fluid layer we also have

$$\Sigma_{31}^f = \frac{\tilde{v}_1(y_3^+) - \tilde{v}_1(y_3^-)}{d_f^0} = -\frac{V_1^{-1}}{d_f^0},$$

providing further justification for Eq. (5.27). Finally with $\mathbf{V}^{-1} = (1 \ 0 \ 0)^\top$ and $y_3 = 0$ without loss the centre of the fluid layer we once more have

$$\tilde{v}_1 = \frac{y_3}{d_f^0} + \frac{1}{2},$$

by reasoning and assumptions in direct analogy with Section A.2.3. The value of $1/2$ in the above expression can be independently confirmed by symmetry when the scaffold has the same geometry in the upper and lower layers, by analogy to the reasoning of Section A.3.